UNIVERSITÀ DI PARMA

UNIVERSITÀ DEGLI STUDI DI PARMA

Dottorato di Ricerca in

Tecnologie dell'Informazione

CICLO XXXVII

Electrification in non-road and road scenarios

Coordinatore:

Chiar.mo Prof. Marco Locatelli

Tutor:

Chiar.mo Prof. Carlo Concari

Co-tutor:

Chiar.mo Prof. Alessandro Soldati

Dottorando: *Marco Bassani*

Anni Accademici 2021/2022 - 2022/2023 - 2023/2024

Summary

List of Figures

List of Tables

Introduction

In recent years, there has been a strong push towards the electrification of vehicles in a broad sense. Every automotive manufacturer currently has at least one electric model on the market.

The electrification of road vehicles is already a relatively mature sector, while other mobility sectors are just beginning their transition towards electrification. One of the sectors that could greatly benefit from this electric transition is that of construction machinery. In this case, replacing or supplementing current internal combustion and hydraulic technologies with equivalent electric solutions can lead to significant advantages in terms of efficiency, reduced environmental impact, and versatility. Electrified construction machines can operate indoor without air pullution. Battery recharging can occur via the electrical grid (plug-in) or through dedicated internal combustion range extenders; in this case, running the internal combustion engine at its most efficient point reduces environmental impact, even if the primary energy source remains fossil fuel.

The electrification of construction machinery brings some challenges, which will be the subject of research in this doctoral project. The ability to use multiple electric machines instead of a single internal combustion engine greatly increases system flexibility and allows for the implementation of innovative control algorithms. Additionally, the replacement of hydraulic components will require an increase in the reliability of the electronic control and drive circuits, which must at least meet the high reliability specifications of current hydraulic systems.

In addition, by electrifying more and more parts of the machine, there is a reduction in noise due to the elimitation of thermal or hydraulic components; however, noise can emerge from electric drives that, despite being of smaller amplitude, falls into the audio band and, being pure notes, can result very annoying. So, along with the project of motor control firmware, a parallel project was born for the need to equip drives with an algorithm for reducing the vibrations due to the cogging torque in order to avoid propagation to the entire powertrain and, thus, reduces the operator's annoyance and, perhaps, prevents the formation of resonance phenomena in the structures which could cause fatigue fails or other negative situations.

For the recharging of construction machines during operation, as mentioned, it is necessary to use an internal combustion range extender. For cars, there is the possibility to think of smarter ad-hoc systems, namely recharging during the movement through an external infrastructure along common routes or in parking areas. Systems with pantographs and overhead lines, like trains and trolleybuses, or systems with sliding brushes under the asphalt, like subways, have already been implemented; however, this penalizes movement flexibility. Additionally, there is the issue that road infrastructures are shared with pedestrians, bicycles, and mopeds, which poses a significant safety concern. A new system that is gaining traction is wireless vehicle charging through the asphalt. As this is a new project, the potential aging effects of asphalt due to strong magnetic fields are still unknown, unlike the aging effects caused by ultraviolet light which are already well understood. A test bench has therefore been created to conduct accelerated tests on samples of bituminous material.

Chapter 1

Fan drive electrification

The design of the entire fandrive system was mainly divided into three key sections. The first involved a theoretical and simulation analysis of the PI controllers, which are fundamental to any control system, comparing the classic architecture with more advanced ones in terms of maintaining steady-state speed and control robustness in case of sudden torque insertion on the shaft. The second section consisted of the development of the firmware and hardware, as well as the creation of the test bench for performing tests and characterizations on the drive. The third section is supplementary and not strictly necessary for the motor's operation, but it was addressed during the project because one of the motors used was found to be very noisy due to vibrations caused by the magnetic interaction between rotor magnets and stator slots. Therefore, an active cogging torque reduction project was initiated to also reduce the generated noise.

1.1 PI regulators synthesis

When designing a control loop, the goal is usually to control a single input variable. To do this, a classic PI controller with one degree of freedom can be used. In the case of the controller used in the current loop, the goal is to control the current on a specific axis analyzing the current error to generate an information about the voltage to be applied along the same axis. For standard speed control, what needs to be controlled is the speed reached by the rotor, and the controller analyzes the speed error to generate a current setpoint to regulate the speed. However, when analyzing the speed loop, there is another input of less importance: the torque disturbance coming from the load. To manage this, it is necessary to add another degree of freedom to the system by adding a prefilter in series to the speed setpoint. The transfer function from speed setpoint to speed can be designed with a low-pass function, considering that the setpoint variations are typically very slow, and to reject any high-frequency disturbances that may enter the speed loop due to cogging torque. Regarding the transfer function from torque disturbance to speed, it is necessary to obtain a function that minimizes the disturbance, thus with a high rejection rate. In particular, a band-pass filter can be implemented to completely reject the effect of counter constant torque at frequencies approaching zero and to effectively reject disturbances caused by cogging torque or from PWM ripple.

1.1.1 Current loop analysis

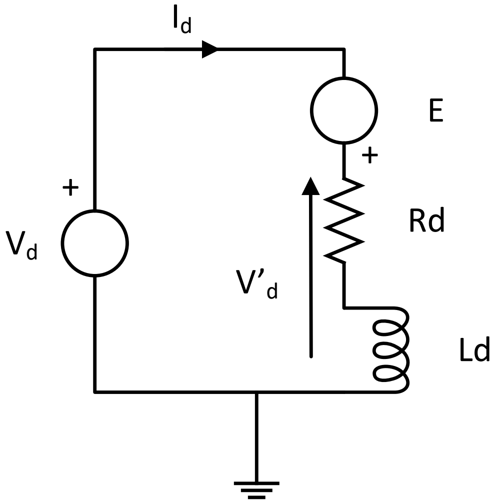

Figure 1.1: Equivalent circuit on d axis of the stator

Considering the motor equivalent circuit Fig. 1.1, $v_d^{'}$ (voltage margin) is the only part of the voltage on d-axis v_d generated by the inverter that can generate torque on the shaft, because when the magnets are rotating, due to the magnetic flux on q axis λ_q, a back electromotive force (BEMF) e is generated, and it reduces this voltage margin:

$$v_d = v_d^{'} - e \tag{1.1}$$

considering, $e = \omega_e \cdot \lambda_q$:

$$v_d = v_d^{'} - \omega_e \cdot \lambda_q \tag{1.2}$$

then the current on the d-axis motor phase is:

$$i_d = \frac{v_d^{'}}{(R_d + s \cdot L_d)} \tag{1.3}$$

with R_d and L_d are respectively the stator resistance and inductance expressed on d-axis.

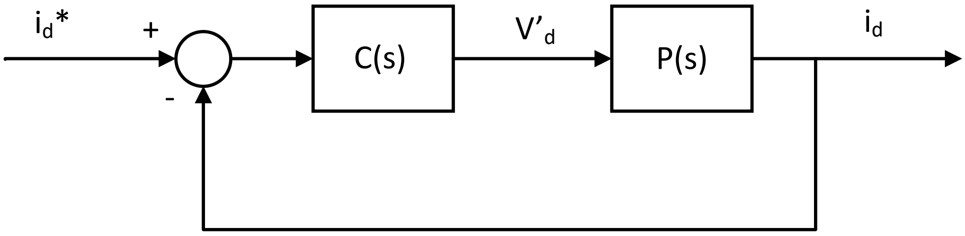

Figure 1.2: Single-wire equivalent path of the current loop on d axis

Analyzing the current loop Fig. 1.2, and considering: the current demand on d axis i_d^*, the $v_d^{'}$ voltage on d-axis computed by the current PI regulator $C_i(s)$, the current absorbed by the motor $P(s)$ on d axis i_d is expressed by:

$$i_d = P(s) \cdot C_i(s) \cdot (i_d^* - i_d) \tag{1.4}$$

with $P(s) = \frac{i_d}{v_d^{'}} = \frac{1}{(R_d + s \cdot L_d)}$ and a general $C_i(s) = \frac{N(s)}{D(s)}$ the transfer function from i_d^* to i_d results:

$$G_{i^*i} = \frac{i_d}{i_d^*} = \frac{P(s) \cdot C_i(s)}{1 + (P(s) \cdot C_i(s))} = \frac{N(s)}{D(s) \cdot (R_d \cdot + s \cdot L_d) + N(s)} \tag{1.5}$$

For the transfer function from i_d^* to i_d of the current loop what we want is a low pass function with the value of the pole angular frequency as high as possible.

Using only a proportional regulator, $N(s) = K_p$, $D(s) = 1$, $C_i(s) = K_p$:

$$G_{i^*i} = \frac{K_p}{R_d + K_p} \cdot \frac{1}{1 + s \cdot \frac{L_d}{R_d \cdot k_p}} \tag{1.6}$$

but a steady state error results.

Now, trying a proportional integral regulator, $N(s) = K_i + K_p \cdot s$, $D(s) = s$, $C_i(s) = K_p + \frac{K_i}{s} = \frac{K_i}{s} \cdot (1 + \frac{k_p}{k_i} \cdot s)$:

$$G_{i^*i} = \frac{\frac{K_i}{s} \cdot (1 + \frac{k_p}{k_i} \cdot s) \cdot \frac{1}{R_d} \cdot \frac{1}{1 + s \cdot \frac{L_d}{R_d}}}{1 + \frac{K_i}{s} \cdot (1 + \frac{k_p}{k_i} \cdot s) \cdot \frac{1}{R_d} \cdot \frac{1}{1 + s \cdot \frac{L_d}{R_d}}} \tag{1.7}$$

forcing $\frac{k_p}{k_i} = \frac{L_d}{R_d}$ it is possible to act a zero pole compensation:

$$G_{i^*i} = \frac{1}{1 + s \cdot \frac{R_d}{K_i}} \tag{1.8}$$

and selecting k_i it is possible to place the pole angular frequency where it is needed, high enough to have a reactive current loop but not too high so that PWM noise is rejected. The constant time of the current loop results $\tau_i = \frac{R_d}{K_i}$. To simplify the speed loop analysis, the G_{i^*i} (1.8) transfer function will become the elementary block of the electric motor plant.

$$P_E(s) = \frac{1}{1 + s \cdot \frac{R_d}{K_i}} = \frac{1}{1 + s \cdot \tau_i} \tag{1.9}$$

1.1.2 Speed loop analysis

In this chapter, it was decided to compare the classic speed loop controlled by a normal PI regulator with 3 other more advanced methods. Starting from the normal loop with one Degree Of Freedom (DOF) PI regulator dedicated to the transfer function (TF) of speed as function of speed set point, we move to controllers with 2-DOF PI in order to also control the effect of a torque disturbance on the speed. In addition, in all cases the type of load connected to the motor is considered, which in this case is a fan and therefore a non-linear load. For each case, after the calibration with a standard fan, we proceeded to perform a Monte Carlo simulation by varying the parameters that constitute the fan characteristic so as to verify the robustness of the various controls when the fans vary due to factory mismatch. Fig. 1.3 shows a classical architecture of a motor speed control loop, with a speed setpoint ω^* expressed in rad/s, the 1-DOF PI $C(S)$ (1.10)

$$C(s) = K_p + \frac{K_i}{s} \tag{1.10}$$

that elaborates the speed error, the electrical contribution of the motor called electrical plant P_E and P_M that is the mechanical plant containing the mechanical part of the motor.

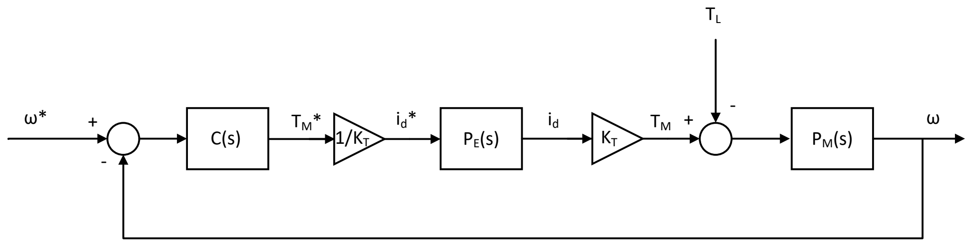

Figure 1.3: Single-wire equivalent path of the speed loop using the theoretical electrical equivalent of the motor

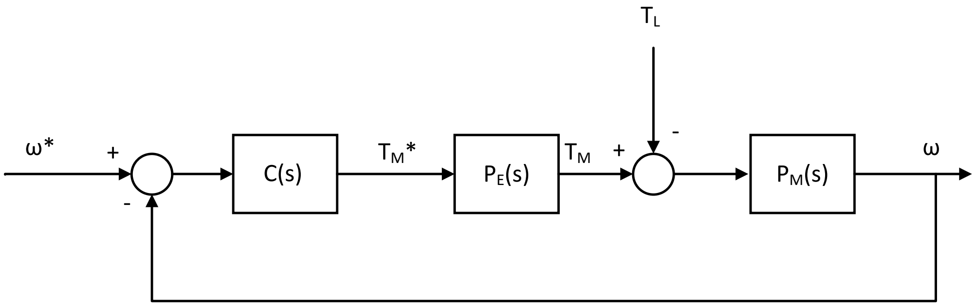

Figure 1.4: Single-wire equivalent path of the speed loop using an electrical equivalent of the motor that includes the torque constant adaptations

T_M^* is the torque demand elaborated by the PI to keep the speed error near to zero and T_M is the real torque that the electrical stator coils generate on the internal part of the rotor. The currents ${i_d}^*$ and i_d are the current demand and the absorbed current on d-axis respectively. The load torque T_L is a potentially applied resistant torque independent from rotor speed, and subtracting it from T_M gives the torque available to counter the friction torque T_F, of shaft wheel bearings and the load in case of linear load, and the torque T_A needed to accelerate the load in case of speed change. For easier analysis, it is preferable to have a representation with only the torque variables shown in Fig. 1.4. The torque balance:

$$T_M - T_L - T_F - T_A = 0 \tag{1.11}$$

considering $T_F = B \cdot \omega$ with B the total friction coefficient (wheel bearings + load), and $T_A = J \cdot \dot{\omega}$ with J the total inertia coefficient (rotor + blades)

$$\begin{aligned} T_M - T_L &= B \cdot \omega + J \cdot \dot{\omega} \\ &= (B + J \cdot s) \cdot \omega \end{aligned} \tag{1.12}$$

considering the output of $P_M(s)$ over its input, and extracting the time constant $\tau_m = \frac{J}{B}$:

$$P_M(s) = \frac{1}{(B + s \cdot J)} = \frac{1}{B \cdot (1 + \tau_m \cdot s)} \tag{1.13}$$

To proceed a simplifying assumption is used in the following analysis, which is the consideration that the current loops are at least two orders of magnitude faster than the entire speed loop, and thus, from the point of view of the speed loop, the pole of the current loop can be neglected and the transfer function of $P_E(s)$ can be considered having a constant magnitude of 1 as in Fig. 1.5

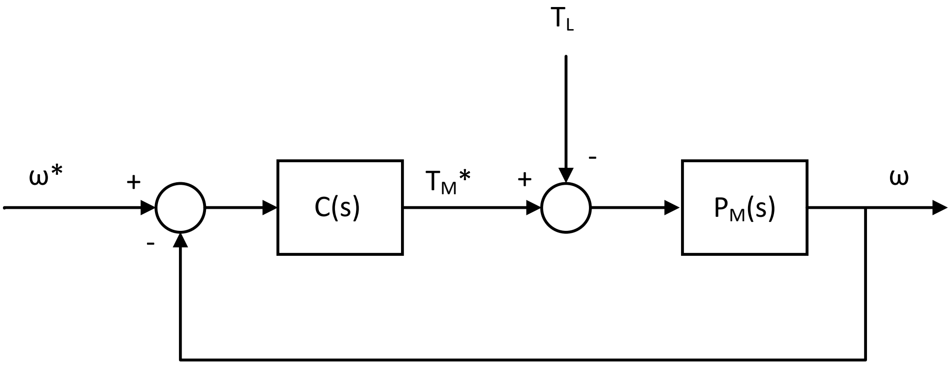

Figure 1.5: Simplified single-wire equivalent path of the speed loop with neglected electrical plant

1.1.3 Real fan fitting

To improve the various types of regulators it was first necessary to obtain the speed-torque function of the fan under test, and not being a linear load as had been initially taken as a hypothesis, it was physically characterized creating a table speed vs. DC power and then through the inverter and motor efficiency it has been possible to extrapolate the torque used by the fan with:

$$torque = \frac{\eta_{tot} \cdot P_{dc}}{\omega_r} \tag{1.14}$$

Table 1.1: Experimental characterization of the fan

Speed (rpm)	Speed (rad)	Power (dc)	Total efficiency	Torque
1100	115.19	100	0.873	0.758
1300	136.14	150	0.873	0.962
1500	157.08	217	0.873	1.206
1700	178.02	300	0.863	1.454
1900	198.97	400	0.882	1.774
2100	219.91	525	0.882	2.107
2300	240.86	695	0.895	2.582
2500	261.80	875	0.887	2.966
2700	282.74	1100	0.895	3.483
2900	303.69	1360	0.885	3.963
3100	324.63	1650	0.885	4.498
3300	345.58	1980	0.885	5.070
3500	366.52	2350	0.885	5.674

Then a fitting in Matlab was performed to obtain a function as faithful as possible. Fig. 1.6 shows experimental values and the fitting curve with a second order function (1.15) with the c term forced to zero to reach a function crossing the zero amplitude at zero speed.

$$T_F = a \cdot \omega_r^2 + b \cdot \omega_r + c \tag{1.15}$$

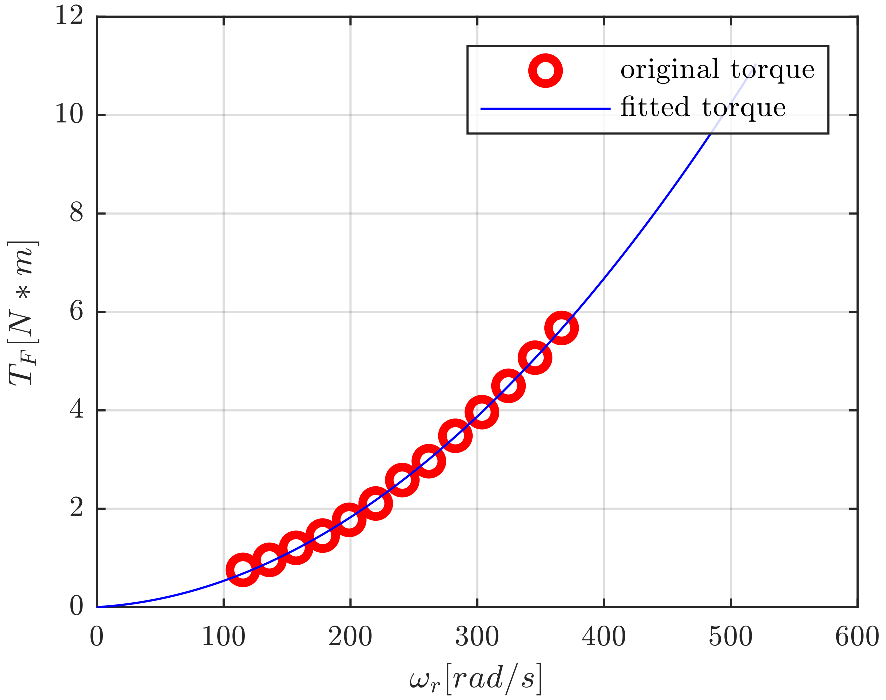

Figure 1.6: Original characterization points and fitted curve passing through zero

To analyze the control with the classical linear model methods, there is the need to linearize the nonlinear function of the fan T_F, and by using the formula for the line passing through a point $(\omega_0, T_F(\omega_0))$ with slope $B(\omega_0)$

$$T_{F,lin} = T_F(\omega_0) + B(\omega_0) \cdot (\omega - \omega_0) \tag{1.16}$$

By differentiating (1.15), $B(\omega) = 2 \cdot a \cdot \omega + b$,

$$T_{F,lin} = (2 \cdot a \cdot \omega_0 + b) \cdot \omega + (c - a \cdot {\omega_0}^2) \tag{1.17}$$

with the friction coefficient

$$B_{lin} = (2 \cdot a \cdot \omega_0 + b) \tag{1.18}$$

and the y-axis intercept offset

$$off_{lin} = (c - a \cdot {\omega_0}^2) \tag{1.19}$$

1.1.4 1-DOF PI

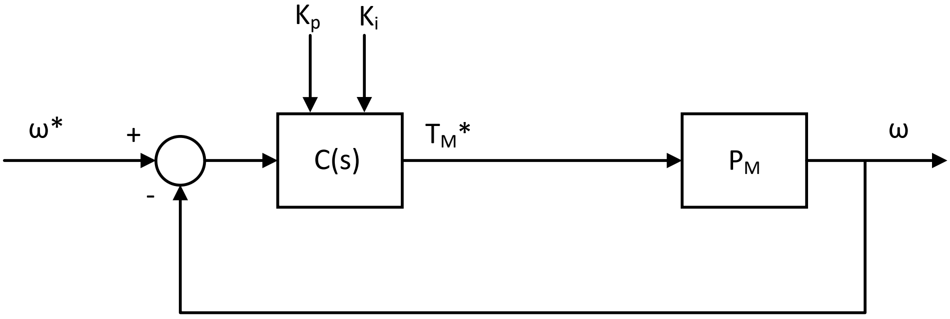

Figure 1.7: Single-wire equivalent path with 1-DOF controller and real mechanical plant not linearized

From Fig. 1.5 the transfer function from ω^* to ω

$$G_{\omega^*\omega} = \frac{C(s) \cdot P_M(S)}{1 + C(s) \cdot P_M(S)} \tag{1.20}$$

using (1.10) and (1.13):

$$G_{\omega^*\omega} = \frac{K_p s + K_i}{Js^2 + (B + K_p)s + K_i} \tag{1.21}$$

with one zero

$$Z_1 = \frac{K_i}{K_p} \tag{1.22}$$

and two poles

$$\begin{cases} P_1 = -\frac{B+K_p-\sqrt{B^2+2BK_p+K_p^2-4JK_i}}{2J} \\ P_2 = -\frac{B+K_p+\sqrt{B^2+2BK_p+K_p^2-4JK_i}}{2J} \end{cases} \tag{1.23}$$

To obtain a low pass function the lower frequency pole P_1 has been canceled with Z_1 finding:

$$K_p = \frac{JK_i}{B} \tag{1.24}$$

Rewriting (1.21):

$$G_{\omega^*\omega} = \frac{K_i}{K_i + B \cdot s} \tag{1.25}$$

a pole remains:

$$P_2 = -\frac{K_i}{B} \tag{1.26}$$

and forcing that pole to be equal to 50 rad/s

$$K_i = 50 \cdot B \tag{1.27}$$

from (1.21):

$$G_{\omega^*\omega} = \frac{50 \cdot B}{50 \cdot B + B \cdot s} \tag{1.28}$$

The value of B is taken considering the linearized fan by (1.18) choosing $\omega_0 = \omega_{0,centr} = 150\,\mathrm{rad/s}$ the middle of the speed range. The final transfer function and coefficients are:

$$G_{\omega^*\omega} = \frac{50}{s + 50} \tag{1.29}$$

$$K_p = 0.6250 \tag{1.30}$$

$$K_i = 0.6459 \tag{1.31}$$

The Simulink simulation has been set with a step speed set-point from zero to $150\,\mathrm{rad/s}$ and inserting a torque demand after a while.

1.1.5 1-DOF PI with torque Feed Forward

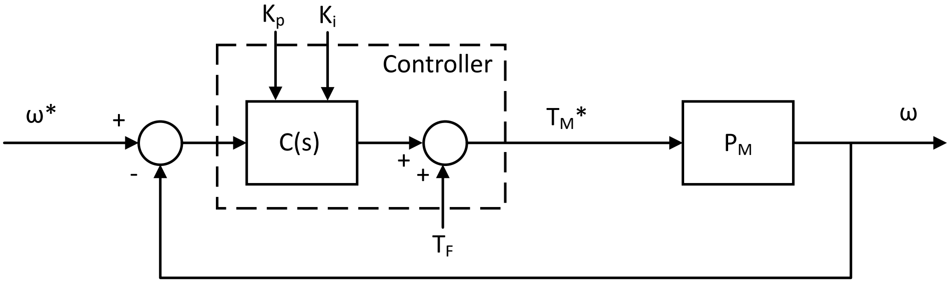

Figure 1.8: Single-wire equivalent path with 1-DOF controller with real fan torque in feed-forward and real mechanical plant not linearized

In this architecture the only change with respect to Fig. 1.7 is a branch added in feed-forward to the output stage of the PI controller with a value of T_F directly from the fitted nonlinear equation (1.15) evaluated in the actual motor speed ω. This modification aims at not overloading the integral part of the regulator and lets it deal only with the correction of the inertial part J in (1.13). From (1.20) to (1.28) the same calculation has been followed, the difference is about the value of B that has to be taken for proportional and integral constant computation, because now it is assumed that the value of B in (1.13) has been totally compensated by the fan torque added in feed-forward and therefore not within the regulator's competence, for this reason, $B = 0$.

$$k_i = 0 \tag{1.32}$$

$$k_p = 0.6250 \tag{1.33}$$

1.1.6 2-DOF PI

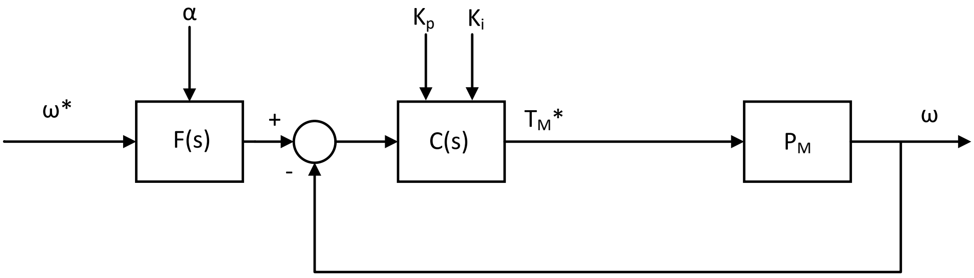

Figure 1.9: Single-wire equivalent path with 2-DOF controller and real mechanical plant not linearized

After the tests on the 1-DOF PI it was decided to explore another way, that of the 2-DOF PI [1], that is the same architecture seen above with the addition of a prefilter that adds a second degree of freedom to be able to manage also the disturbance to the motor speed caused by load torque, in such a way that the speed of the motor is as unaffected as possible by any sudden torque demand due to, for example, strong air turbulence.

A prefilter has been added in series to the input speed set point ω^*:

$$F = -\frac{T_i s(\alpha - 1) + DT_d T_i s(\beta - 1) - 1}{T_i s + DT_d T_i s + 1} \tag{1.34}$$

considering $D = s$, $T_i = K_p/K_i$, $T_d = K_d/K_p$ and $K_d = 0$ to not use the derivative factor:

$$F = \frac{(K_p - K_p \cdot \alpha)s + K_i}{K_p s + K_i} \tag{1.35}$$

We start from the transfer function from ω^* to ω as in the case of the 1-DOF regulator:

$$G_{\omega^*\omega} = F(s) \cdot \frac{C(s) \cdot P(S)}{1 + C(s) \cdot P(S)} \tag{1.36}$$

using (1.10) and (1.13):

$$G_{\omega^*\omega} = \frac{K_i + s \cdot (K_p - K_p \cdot \alpha)}{Js^2 + (B + K_p)s + K_i} \tag{1.37}$$

resulting in one zero:

$$Z_1 = -\frac{K_i}{K_p - K_p \cdot \alpha} \tag{1.38}$$

and two poles:

$$\begin{cases} P_1 = -\frac{B+K_p-\sqrt{B^2+2BK_p+K_p^2-4JK_i}}{2J} \\ P_2 = -\frac{B+K_p+\sqrt{B^2+2BK_p+K_p^2-4JK_i}}{2J} \end{cases} \tag{1.39}$$

forcing the zero pole cancellation with the lower frequency pole: $P_1 = Z_1$ yields the value of α for the prefilter tuning:

$$\alpha = \frac{K_p - \frac{2JK_i}{B+K_p-\sqrt{B^2+2BK_p+K_p^2-4JK_i}}}{K_p} \tag{1.40}$$

the remaining pole is:

$$P_2 = -\frac{2K_i}{B + K_p - \sqrt{B^2 + 2BK_p + K_p^2 - 4JK_i}} \tag{1.41}$$

and forcing the pole $P_2 = \omega_{h\_ww}$ that is the value of angular frequency which has been chosen for the high-frequency pole, an expression for K_i is found:

$$K_i = B \cdot \omega_{h\_ww} + K_p \cdot \omega_{h\_ww} - J \cdot \omega_{h\_ww}^2 \tag{1.42}$$

Now considering the transfer function from torque to speed:

$$G_{\omega t} = -\frac{P}{1 + (P \cdot C \cdot EL)} = -\frac{s}{Js^2 + (B + K_p)s + K_i} \tag{1.43}$$

there is one zero in the origin:

$$Z_0 \tag{1.44}$$

and two poles:

$$\begin{cases} P_1 = -\frac{B+K_p-\sqrt{B^2+2BK_p+K_p^2-4JK_i}}{2J} \\ P_2 = -\frac{B+K_p+\sqrt{B^2+2BK_p+K_p^2-4JK_i}}{2J} \end{cases} \tag{1.45}$$

placing k_i (1.42) in (1.43):

$$G_{\omega t} = -\frac{s}{B\cdot\omega_{h\_ww} + s\cdot(J\cdot\omega_{h\_ww} + J\cdot P_{tw\_H}) - J\cdot\omega_{h\_ww}^2 + J\cdot s^2 + \omega_{h\_ww}\cdot(J\cdot\omega_{h\_ww} - B + J\cdot P_{tw\_H})} \tag{1.46}$$

the two poles become:

$$\begin{cases} P_1 = -\omega_{h_w w} \\ P_2 = -\frac{(B+K_p-J*\omega_{h_w w})}{J} \end{cases} \tag{1.47}$$

and forcing $P_2 = -P_t w_H$ it results:

$$K_p = J\cdot\omega_{h\_ww} - B + J\cdot P_{tw\_H} \tag{1.48}$$

and selecting the angular frequency of the low pass function of $G_{\omega^*\omega}$, $\omega_{h_w w} = 50\,\mathrm{rad/s}$ and the angular frequency of the higher frequency pole of $G_{\omega t}$, $P_{h_t w} = 250\,\mathrm{rad/s}$, and the value of B considering the linearized fan by (1.18) choosing $\omega_0 = \omega_{0,centr} = 150\,\mathrm{rad/s}$ the middle of the speed range, it results:

$$K_p = 3.75 \tag{1.49}$$

$$K_i = 156.25 \tag{1.50}$$

$$\alpha = 0.166 \tag{1.51}$$

$$G_{\omega^*\omega} = \frac{625}{2\cdot(\frac{5s}{4}+\frac{625}{2})} \tag{1.52}$$

$$G_{\omega t} = -\frac{s}{\frac{s^2}{80}+\frac{15s}{4}+\frac{625}{4}} \tag{1.53}$$

1.1.7 Adaptive 2-DOF PI

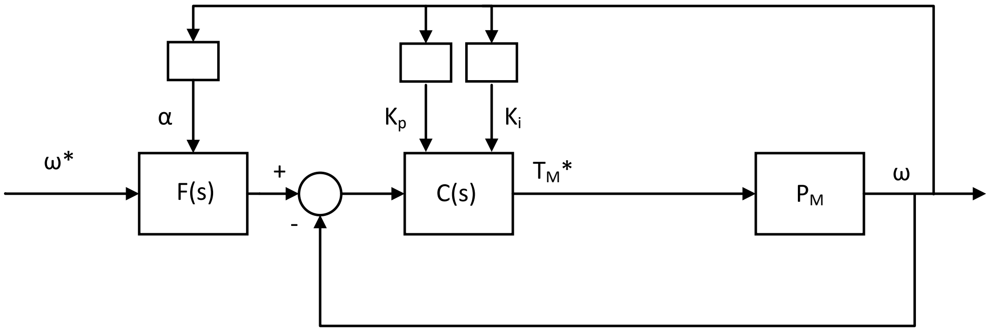

Figure 1.10: Single-wire equivalent path with 2-DOF controller, adaptive filters coefficients, and real mechanical plant not linearized

The calculations are the same as the 2-DOF controller, except for the final numeric results of K_p, K_i, and α that are not evaluated at fixed speed but evaluated iteratively based on motor speed.

$$K_p = 3.75 - 75.64 \cdot 10^{-6} \cdot \omega_r \tag{1.54}$$

$$K_i = 3.78 \cdot 10^{-3} \cdot \omega_r + 155.7 \tag{1.55}$$

$$\alpha = 1.0 - \frac{1.045}{0.000076 \cdot \omega_r - \left(0.000565 \cdot \omega_r + (0.000076 \cdot \omega_r + 0.00157)^2 + 6.165\right)^{1/2} + 3.739} \tag{1.56}$$

To verify the robustness level of the various controllers analyzed, it is necessary to test them with loads (fans) that deviate from the ideal values used for tuning the coefficients. To achieve this, Monte Carlo simulations were prepared in MATLAB to run simulations with different fans. To generate fans with mismatches due to production processes, new values of a and b were generated using a normal distribution, with the mean value equal to the actual a and b value and a variance of 10% of the mean. Additionally, to exclude faulty fans, a cutoff was applied at 3 sigma, ensuring the generation of 99.73% of possible fans.

The original fan linearized torque with c parameters forced to zero:

$$T = a \cdot \omega_r^2 + b \cdot \omega_r \tag{1.57}$$

and the torque calculated with a and b coefficients coming from normal distribution generation:

$$T = a_{mont} \cdot \omega_r^2 + b_{mont} \cdot \omega_r \tag{1.58}$$

$$\begin{cases} \mu_a = a \\ \mu_b = b \end{cases} \tag{1.59}$$

$$\begin{cases} \sigma_a = 10\% \mu_a \\ \sigma_b = 10\% \mu_b \end{cases} \tag{1.60}$$

$$\begin{cases} \mu_a - 3 \cdot \sigma_a < a_{mont} < \mu_a + 3 \cdot \sigma_a \\ \mu_b - 3 \cdot \sigma_b < b_{mont} < \mu_b + 3 \cdot \sigma_b \end{cases} \tag{1.61}$$

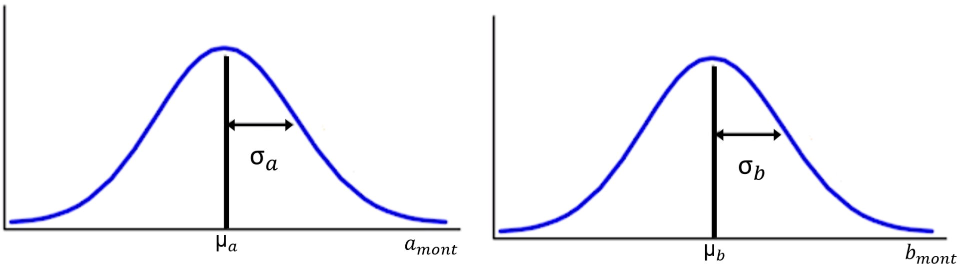

Figure 1.11: Generation of the value of a and b for Monte Carlo tests

For each control architecture and for each Monte Carlo run Fig. 1.12 the initial speed setpoint has been set at 90 rad/s to stabilize the motor and at 0.5 s a speed setpoint variation has been set; after a while at 0.75 s, the error speed value has been recorded to create a steady state statistic. At 0.8 s a second test was performed inserting an instantaneous torque demand, and at 1 s the error speed value has been recorded to create the statistic of torque disturbance rejection.

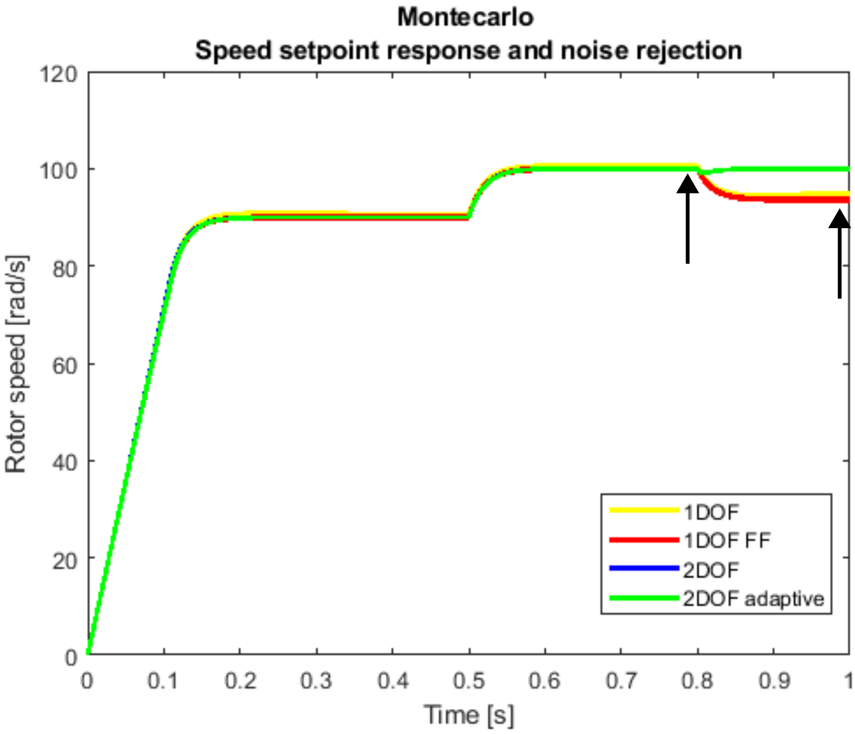

Figure 1.12: Monte Carlo speed setpoint response and noise rejection

In Fig. 1.13 left are shown the histograms of the various error speed values in steady state sampled in Fig. 1.12 at 0.75 s and it can be seen that in the case of 2-DOF controllers the distribution of the speed drop pattern is very little spread and very close to zero rad/s. In Fig. 1.13 right is shown the cropped slice across zero rad/s value to appreciate the distributions of 2-DOF and 2-DOF adaptive controllers.

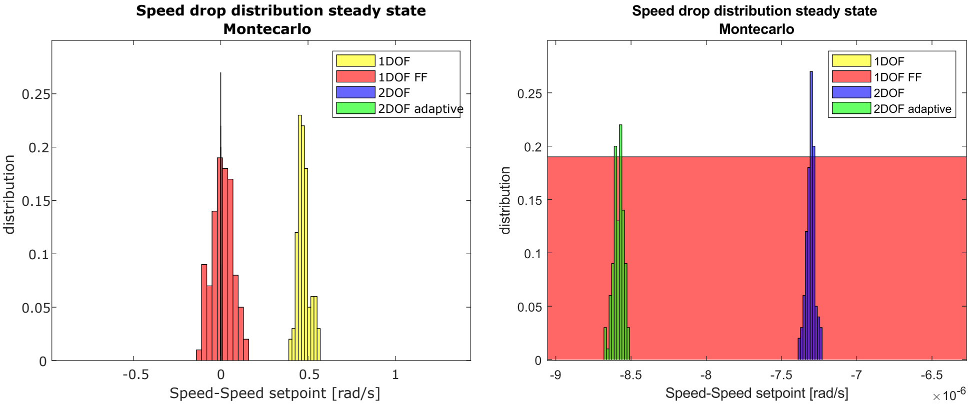

Figure 1.13: Steady state speed distribution

In Fig. 1.14 left are shown the histograms of the various error speed values in case of abrupt request of torque sampled in Fig. 1.12 at 1 s and it can be noticed also in this case, that in the 2-DOF controllers architecture, the distribution of the speed drop is very little spread and near to zero rad/s. In Fig. 1.13 right is shown the cropped slice across $-0.8\,\mathrm{rad/s}$ to appreciate the distributions of 2-DOF and 2-DOF adaptive controllers.

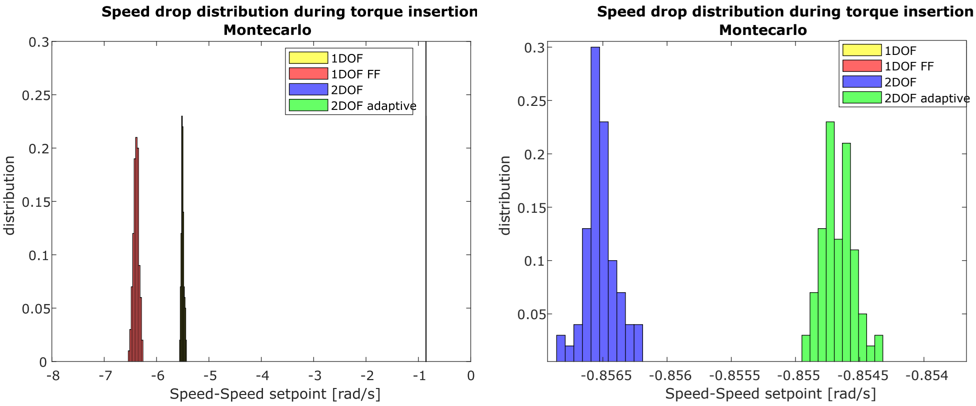

Figure 1.14: Speed drop distribution during torque insertion

1.1.8 Results

Analyzing both statistics, it is evident that solutions with 2-DOF regulators achieve better results with lower steady-state error, lower speed drops under torque insertion, and reduced variance, demonstrating significant independence from variations in the fan. Considering the application on a fan drive and the implementation on a microcontroller with certain constraints, it was decided to use the classic architecture with a 1-DOF regulator for the first release, showing a steady state error of only $0.5\,\mathrm{rad/s}$ compared to a setpoint of $100\,\mathrm{rad/s}$, and a drop of $5.5\,\mathrm{rad/s}$ in the case of a step torque insertion of $4\,\mathrm{N\,m}$ considering the maximum motor torque of $9\,\mathrm{N\,m}$. For a second release, and in case of reusing the same firmware for controlling motors used in applications that require greater precision, the architecture with the adaptive 2-DOF regulator will be taken into consideration.

1.2 Fan drive design

Construction machines generally make extensive use of hydraulic cylinders, as they are actuators with an extremely high torque density and reliability. Consequently, hydraulic motors have also been widely used for rotary actuators due to their simplicity of control and high reliability. With the new electrification paradigm, there is a desire to begin electrifying all rotary actuators, leaving the electrification of hydraulic cylinders, which are still difficult to replace, for last. In collaboration with Casappa S.p.A., a leader in the design and production of hydraulic motors and pumps, it was decided to initiate an electrification experiment for the motors of fan drives (currently driven by hydraulic motor or transmission belt) used for cooling the hydraulic oil radiators of construction machines, before moving on to electrifying all other drives, up to the electrification of the traction motors.

The development of the fan drive was a challenge from many perspectives because the goal was to create an integrated drive, with the inverter fully inside the motor, resulting in a compact and easy-to-install system. This also allows for retrofitting on already constructed machines, requiring only a 48 VDC power supply directly from the batteries and a CAN-BUS communication link. This necessitated the design of an inverter capable of operating at very high ambient temperatures, given its proximity to hydraulic circuits (up to 80 degrees Celsius), delivering 3 kW of power with phase currents on the order of 100 A (due to the use of traditional lead-acid batteries, as lithium power packs were not yet ready), and functioning in both directions up to speeds of 3500 rpm. Additionally, it was decided to eliminate the position/speed sensor by implementing a rotor speed estimation algorithm for sensorless control to enhance reliability.

1.2.1 Hardware

Initially, it was decided to create a 5 kW drive, equivalent to the power of the hydraulic motor being replaced. Together with the company, the first inverter was designed without focusing too much on compactness due to COVID-related difficulties in sourcing components and also to aid in debugging possible problems. We needed a starting platform to quickly test the developed firmware and the first components are shown in Fig. 1.15, Fig. 1.16, Fig. 1.17.

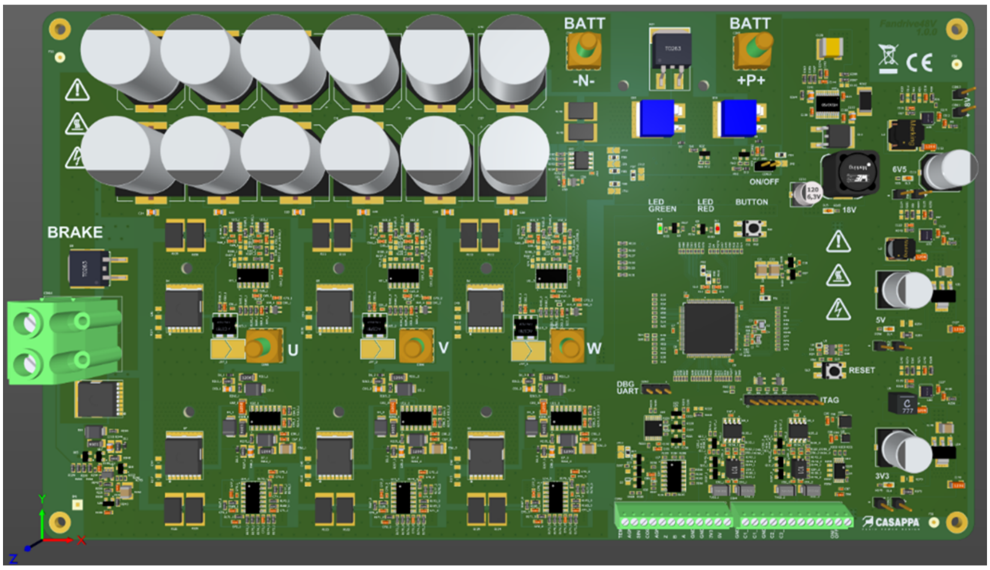

Figure 1.15: First inverter prototype 5 kW rated

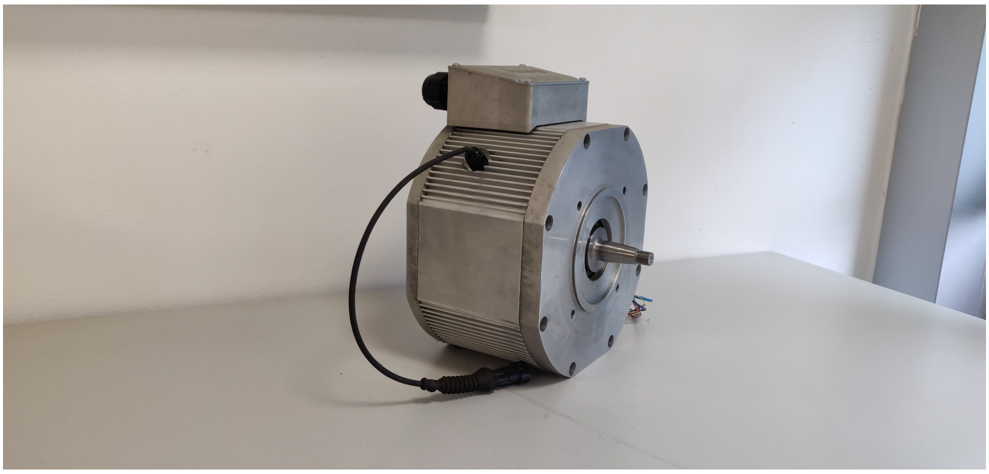

Figure 1.16: First motor prototype 5 kW rated

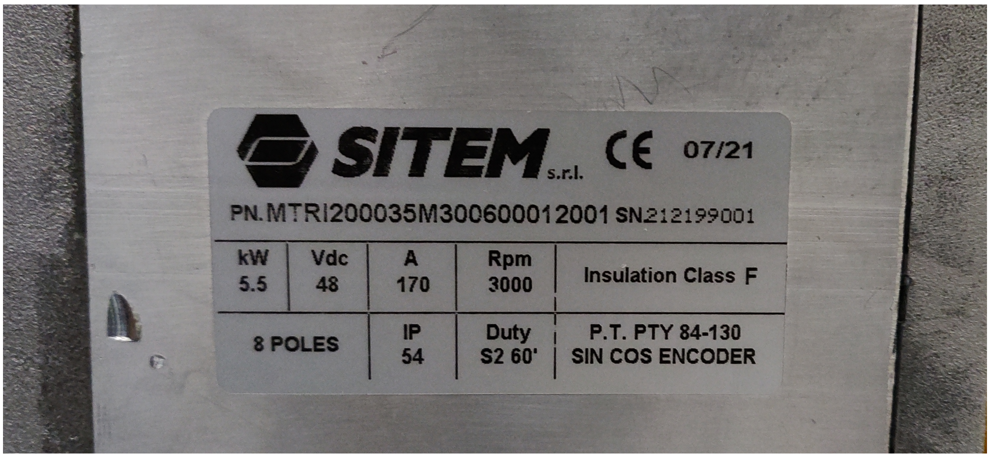

Figure 1.17: 5 kW Motor nameplate

For the second prototype, a size of 3 kW was considered for both the motor and inverter Fig. 1.18, Fig. 1.19, Fig. 1.20, as the 5 kW motor had a larger diameter than the fan core and obstructed too much airflow. A third inverter prototype was then developed with some circuit improvements, together with a third motor prototype.

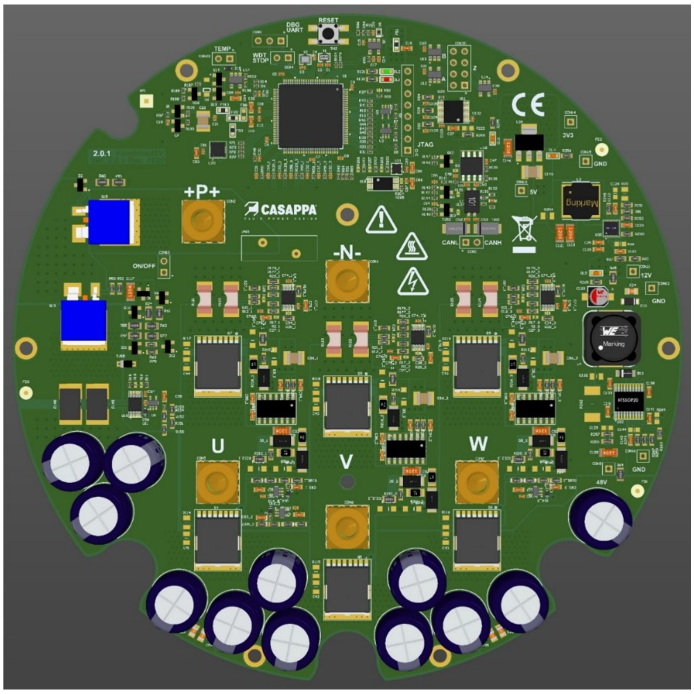

Figure 1.18: Second and third inverter prototype 3 kW rated

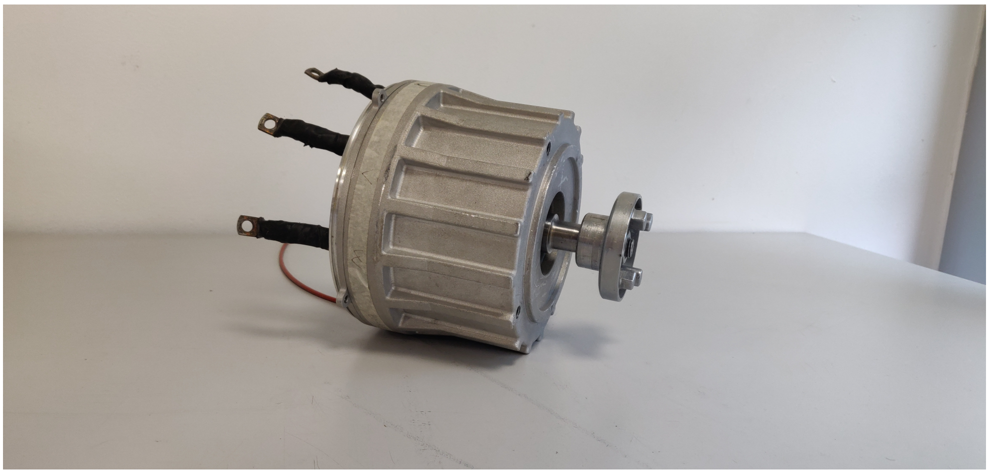

Figure 1.19: Second motor prototype 3 kW rated

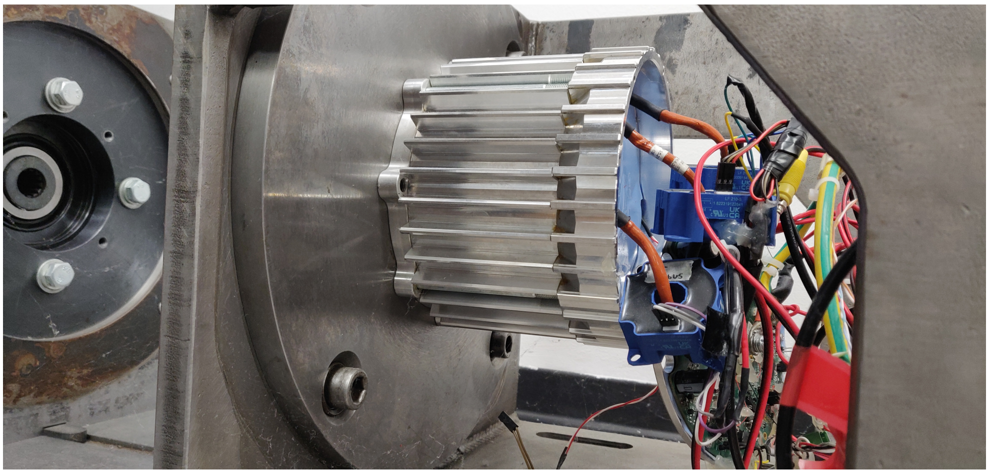

Figure 1.20: Third motor prototype 3 kW rated

Table 1.2: Motors characteristics

	Nominal current (RMS) A	**Nominal power W**	**Nominal speed rpm**	**Nominal torque Nm**	**Torque constant Nm/A**	**Voltage constant V/rpm**	**Stator resistance Ω**	**Stator inductance mH**	**Pole pairs**
Motor 1	170	5500	3000	17.5	0.1	0.0066	-	-	4
Motor 2	64	2500	3500	7	0.11	0.007	-	-	4
Motor 3	58	3000	3500	8.1	0.14	0.0087	0.0082	0.032	4

The overall system has been thoroughly tested on the motor test bench of Fig. 1.21.

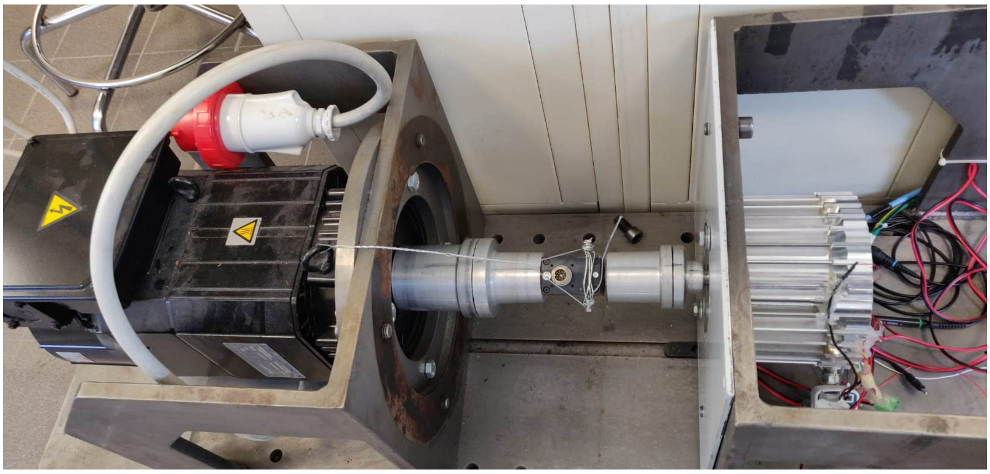

Figure 1.21: Motor test bench (braking bench)

A commercial inverter Fig. 1.22 has been programmed to control the brake motor in constant torque mode and thanks to an analog data acquisition board, torque meter, Hall effect current sensors, and an analog front end of Fig. 1.24 and Fig. 1.25, it has been possible to acquire all the variables and analyze the performance. It was also possible to do some deep fail tests under a strong stress condition, even in overload and overspeed situations. The core of the measures is the analog to digital acquisition board National Instruments PCIe-6353, fitted inside the dedicated PC, equipped with a single analog to digital converter with 16 bit of resolution, a sample rate of 1 MS/s shared for 32 analog input, and the input range of ±10 V.

Figure 1.22: Commercial motor test bench inverter, Emerson UNIDRIVE

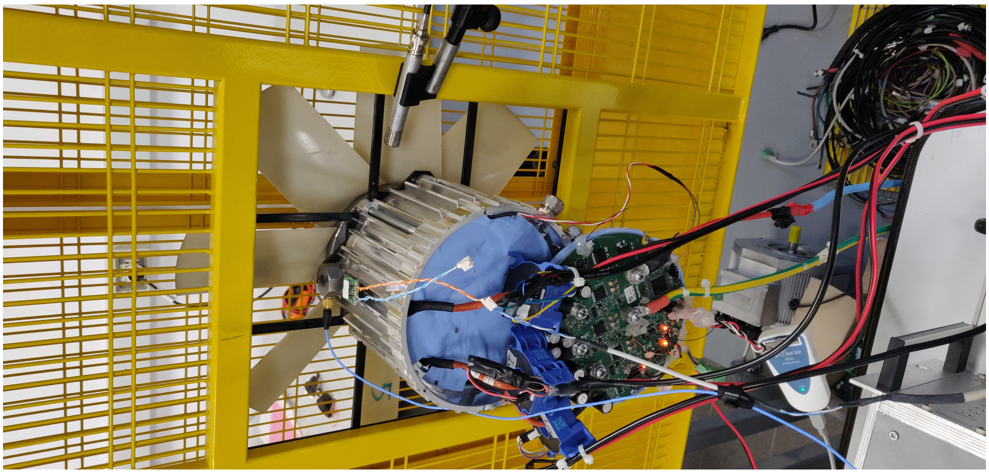

Figure 1.23: Fan drive real application

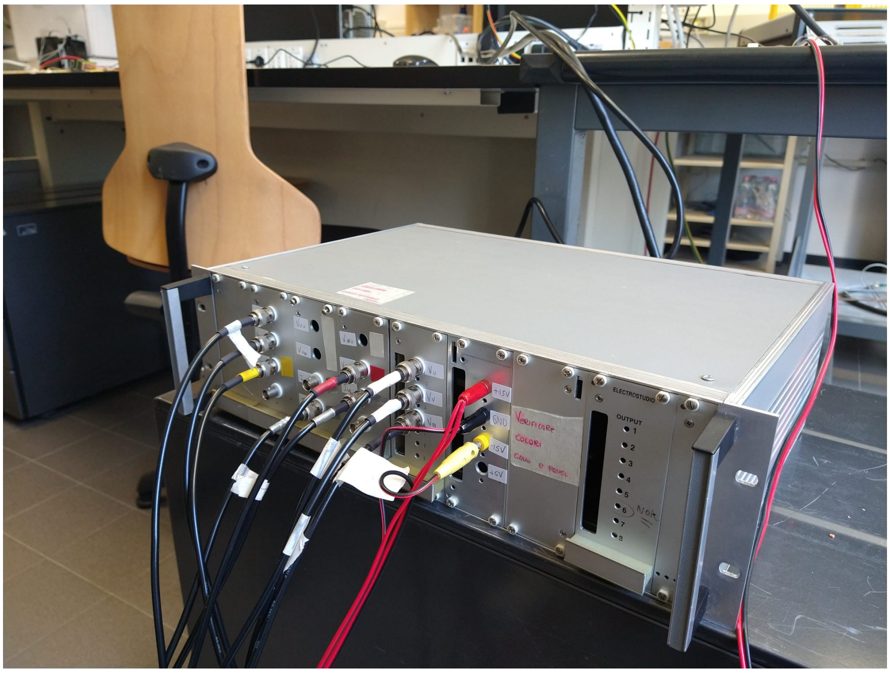

Figure 1.24: Analog front-end for motor characterization

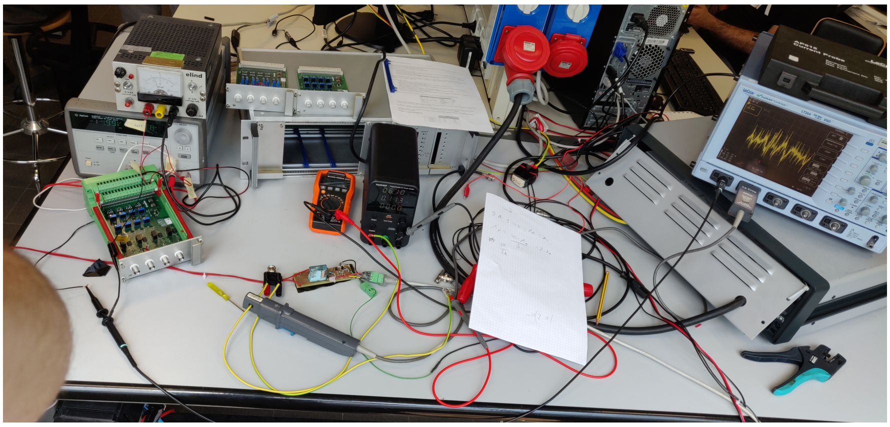

Figure 1.25: Analog front-end calibration

Table 1.3: Transducers and front-end characteristics

	Input range	**Input typology**	**Transducer**
$V_u V_v V_w$ Phase to star center voltages	0-100 V	isolated	From RC filter for PWM ripple elimination R= $1.4\,\mathrm{k\Omega}$, C= $50\,\mathrm{nF}$, $f_{3dB} = 2.27\,\mathrm{kHz}$
V_{bus} DC bus voltage	0-100 V	isolated	From inverter capacitors
$I_v I_w$ Phase current	±5 A	non isolated	LEM, LF 210-S, current gain = 1/2000
I_{bus} DC bus current	0-100 mA	non isolated	LEM, LF 210-S, current gain = 1/2000
T Rotor mechanical torque	±5 V	non isolated	Dr. Staiger Mohilo, 0170/01 MS 50 RA, range ±50 Nm
ω_r Rotor mechanical speed	±10 V	non isolated	Emerson UNIDRIVE motor test bench inverter with analog output speed range ±10 V

1.2.2 Mathematical approach

For this project, a surface permanent magnet synchronous motor (SPMSM) was used to achieve high efficiencies using field-oriented control (FOC) Fig. 1.26 and to attain high torque densities. Therefore, a smaller diameter will result in greater air flow from the fan drive. Directly controlling the sinusoidal currents of an AC machine is notably difficult, so it is common practice to transform the three-phase sinusoidal quantities on axes U-V-W into constants (at steady state) using the Clarke-Park transformations, projecting the sinusoidal quantities on rotating axes d and q. The control was implemented on an STM32 ARM-Cortex 32-bit microcontroller.

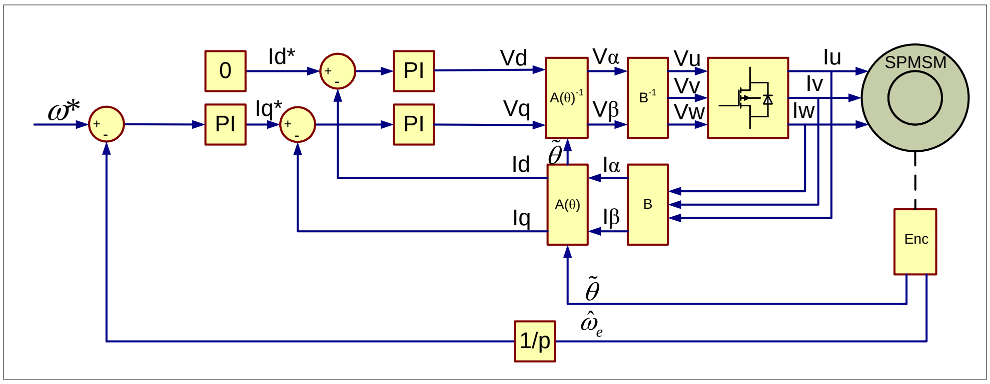

Figure 1.26: Sensored motor control

Fig. 1.26 shows a block diagram of the control, a classical field-oriented control (FOC) on d-q axes. Dealing with the Clarke matrix there is the possibility of correcting it with a constant gain K_B to maintain the value of the power between the U-V-W and d-q representations $(K_B = \sqrt{\frac{2}{3}})$ or maintain the amplitudes of voltages and currents between the two worlds $(K_B = \frac{2}{3})$.

$$[B] = K_B \begin{pmatrix} 1 & -\frac{1}{2} & -\frac{1}{2} \\ 0 & \frac{\sqrt{3}}{2} & -\frac{\sqrt{3}}{2} \\ \frac{1}{\sqrt{2}} & \frac{1}{\sqrt{2}} & \frac{1}{\sqrt{2}} \end{pmatrix} \tag{1.62}$$

In an application such as those with an isolated star center connection, it is evident that the algebraic sum of currents is zero so the line of homopolar components in Clarke matrix can be neglected, the (1.62) can be rewritten:

$$[B] = K_B \begin{pmatrix} 1 & -\frac{1}{2} & -\frac{1}{2} \\ 0 & \frac{\sqrt{3}}{2} & -\frac{\sqrt{3}}{2} \end{pmatrix} \tag{1.63}$$

(1.63) transforms three-phase quantities in a U-V-W reference frame into a dual-phase representation on a dual-phase orthogonal reference frame α-β. Adding the Park transformation matrix $[A]$

$$[A(\theta)] = \begin{pmatrix} \cos\theta & \sin\theta \\ -\sin\theta & \cos\theta \end{pmatrix} \tag{1.64}$$

it eases the control by turning the α-β fixed-axes representation in a rotating-axes representation on axes d-q. This renders the quantities (voltages, currents, fluxes) constant (in stationary conditions) so that they can be managed better by the control. By exploiting the inverse matrices $[A^{-1}]$ $[B^{-1}]$ it is possible to close the current control loops going back and transform from I_d I_q useful for the control into I_U I_V I_W for driving the motor. To control the torque of the motor it is useful to find the relations between torque and current/voltages on d-q axes, therefore the general model of the motor on the d–q axes is derived from the following equations:

$$\begin{cases} v_d = R \cdot i_d + \frac{d\lambda_d}{dt} - \omega_e \cdot \lambda_q \\ \lambda_d = L_d \cdot i_d + \lambda_{m,d} \\ v_q = R \cdot i_q + \frac{d\lambda_q}{dt} + \omega_e \cdot \lambda_d \\ \lambda_q = L_q \cdot i_q + \lambda_{m,q} \end{cases} \tag{1.65}$$

where v_d and v_q are the voltages on the d–q axes; i_d and i_q are the currents on the d–q axes; R is the stator resistance; L_d and L_q are the stator inductances on the d–q axes, respectively; λ_d, λ_q are the stator magnetic fluxes on the d–q axes produced by the d–q currents; $\lambda_{m,d}$, $\lambda_{m,q}$ are the fluxes produced by rotor magnets; and ω_e is the electrical speed. Rewriting the (1.65) using Laplace transformation, and considering the hypothesis of isotropic motor, $(Ld = Lq = Leq)$:

$$\begin{cases} v_d = R \cdot i_d + s \cdot \lambda_d - \omega_e \cdot \lambda_q \\ \lambda_d = L_{\text{eq}} \cdot i_d + \lambda_{m,d} \\ v_q = R \cdot i_q + s \cdot \lambda_q + \omega_e \cdot \lambda_d \\ \lambda_q = L_{\text{eq}} \cdot i_q + \lambda_{m,q} \end{cases} \tag{1.66}$$

Under the hypothesis that $\lambda_{m,d}$, $\lambda_{m,q}$ are not time-dependent, the expression of v_d and v_q can be rewritten:

$$\begin{cases} v_d = R \cdot i_d + s \cdot L_{\text{eq}} \cdot i_d - \omega_e \cdot \left(L_{\text{eq}} \cdot i_q + \lambda_{m,q}\right) \\ v_q = R \cdot i_q + s \cdot L_{\text{eq}} \cdot i_q + \omega_e \cdot \left(L_{\text{eq}} \cdot i_d + \lambda_{m,d}\right) \end{cases} \tag{1.67}$$

In the same way, the mechanical torque can be expressed:

$$T = p \cdot (\lambda_d \cdot i_q - \lambda_q \cdot i_d) \tag{1.68}$$

where p is the pole pairs of the motor. Using (1.66).b and (1.66).d:

$$T = p \cdot \left[\left(L_{\text{eq}} \cdot i_d + \lambda_{m,d} \right) i_q - \left(L_{\text{eq}} \cdot i_q + \lambda_{m,q} \right) i_d \right] \tag{1.69}$$

and thanks to the alignment of the rotor magnet along the d-axis resulting from the field-oriented control, we can see that the torque is proportional to the current iq.

$$T = p \cdot \lambda_{m,d} \cdot i_q \tag{1.70}$$

The control is made by two symmetrical internal loops that control the desired currents on d-q axes with an external speed loop that regulates the motor speed to follow the reference speed. Both the current loops consist of an input set-point of current ${I_d}^*$ or ${I_q}^*$ from which the value of instantaneous current I_d or I_q read by sensors is subtracted thus obtaining the current errors. Once the current error is obtained it can be used to compute the voltage level to be applied to the inverter to obtain the desired current by means of the proportional-integral current controllers. As can be seen in (1.70) for the normal operations of the motor, the torque is controlled only by I_q and then we can set ${I_d}^* = 0$ and feed ${I_q}^*$ with an information that depends on the speed demand of the user. The architecture of the speed loop is the same as those of the currents, the information about instantaneous speed ω is subtracted to the user speed setpoint ω^* obtaining the speed error that, once elaborated by a PI regulator, becomes the information of current setpoint on q axis ${I_q}^*$ for the control of the torque. In section 1.1 the controllers will be illustrated and different architectures will be analyzed and compared. Initially, it was decided to develop a sensor-driven control with an encoder in order to design a reliable and working control, after which it was decided to eliminate it to obtain a less expensive and more reliable drive and rely on an algorithm for estimating the rotor speed by use of speed observer exploiting the reading of the back electromotive forces on the current read by current sensors (shunt).

1.2.3 Encoder reading

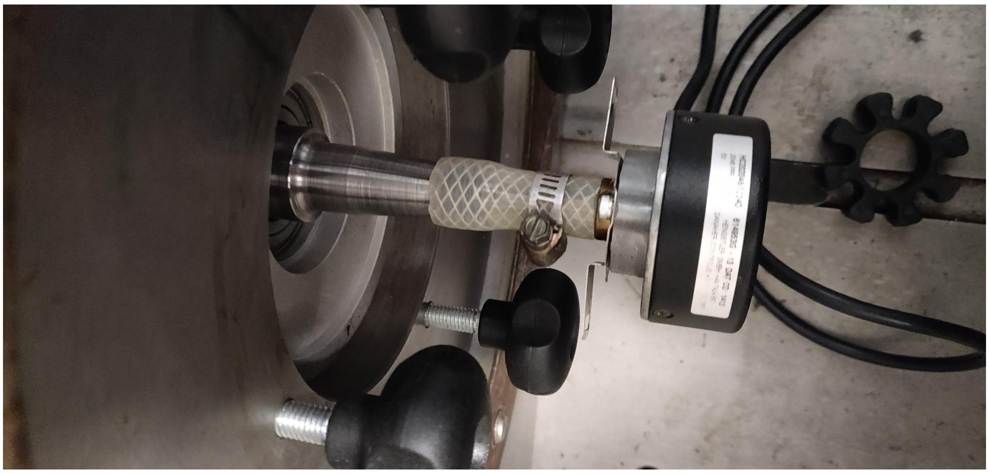

Figure 1.27: Encoder

For the phase information to be used in the sine and cosine function used in Park matrix, there is the need to wrap the angle around $-\pi$ rad and $+\pi$ rad to automatically eliminate the angle multiplicity. It is convenient to use the timer peripheral in "encoder mode" to track the position using the two channels-quadrature incremental encoder. That peripheral is driven mainly by two registers, the counter and the period registers, the first is the one that is increased or decreased for each event of rising and falling edge of both channels. The second one is the register that contains the end of the count value to provide the restart of the counting value to ensure the angle wrapping. That said, for the correctness of the control it is necessary to consider only the electric angle, so taking into account the number of pole pairs p of the motor, the number of pulses per mechanical round n, the value to be inserted into period register is (1.71).

$$period = (\frac{n \cdot 4}{p}) - 1 \tag{1.71}$$

In that way, the counter register shows a sawtooth trend between zero and $(period - 1)$, with some additional normalization it is possible to adapt it to obtain the position angle.

$$radians\_encoder\_angle = \pi \cdot (counter - \frac{period}{2}) \tag{1.72}$$

The speed was determined using a timer peripheral of the microcontroller driven by one of two signals from the encoder, and the available methods are practically two:

- Counting the number of encoder events that occur in a time unit, but having to size the clock, prescaler, and period register of the timer peripheral in order to not overflow at the maximum speed to be reached, that method leads to reach good speed definition at high speed but poor definition at very low speed.
- Counting the elapsed time between each two encoder events, in that case, to prevent the counter register overflow, the size of the clock, prescaler, and period registers are made considering the minimum speed of interest, but in that method, we have the reverse problem, high definition at very low speed and poor definition at high speed. You may also have an additional problem with the speed updating ratio because it changes with different dynamics according to the instantaneous speed of the motor, which in particular applications could be a problem.

In this project, it was decided to use the second method because it is fully manageable by the timer peripheral as to not have any random delay or either overload the code with a high number of interrupt requests coming from the encoder. Since the application of this drive is to control a fan that has an approximate speed-torque curve between the second and third order, it is not of interest to work at low speed as it would not provide any significant airflow.

The sensored control has been useful for the development of current reading peripherals and the whole mathematical algorithm to be ready for the implementation of the sensorless algorithm.

1.2.4 Sensorless algorithm

For the sensorless algorithm, the choice went to a model reference adaptive system (MRAS) architecture [2] because it works well in high-speed applications and it doesn't complicate too much the control as some architecture with an injection of current which is mainly composed of three blocks Fig. 1.28, reference model, adaptive model and adaptive law. The goal of this kind of algorithm is to reach the match of the adaptive model and the reference model through an adaptive law.

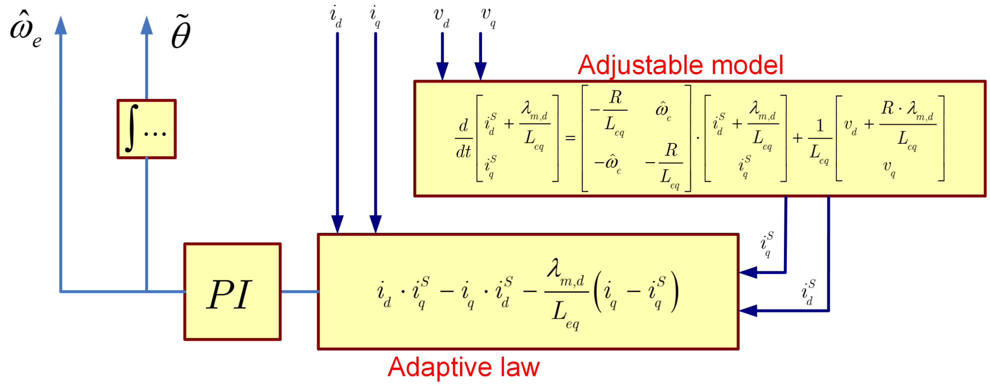

Figure 1.28: Sensorless algorithm

The mathematical model of the stator current for PMSM on d-q axes was chosen as the adjustable model, then taking in input the values of the voltages on d-q axes V_d, V_q well known by the modulation index coming from the running firmware and the estimated electrical speed $\hat{\omega}_e$ coming from the feedback loop, it outputs the information about estimated current on d-q axes $\hat{I}_d$ and $\hat{I}_q$. Instead, the physical PMSM is chosen as the reference model, powered by the currents I_d I_q (and through conversion matrices it means I_U I_V I_W), in the output of that block we find the mechanical shaft characterized by its own mechanical speed ω_r to be estimated by the algorithm after a pole pairs correction. The adaptive law aims to process through a mathematical model and a PI regulator both real currents I_d I_q and estimated ones $\hat{I}_d$ and $\hat{I}_q$ in order to accurately estimate the electrical speed of the motor $\hat{\omega}_e$. Under the hypothesis of rotor magnet aligned along d axis and therefore

$$\lambda_{m,q} = 0 \tag{1.73}$$

(1.67) can be rewritten as:

$$\begin{cases} v_d = R \cdot \hat{i}_d + s \cdot L_{\text{eq}} \cdot \hat{i}_d - \omega_e \cdot L_{\text{eq}} \cdot \hat{i}_q \\ v_q = R \cdot \hat{i}_q + s \cdot L_{\text{eq}} \cdot \hat{i}_q + \omega_e \cdot \left(L_{\text{eq}} \cdot \hat{i}_d + \lambda_{m,d} \right) \end{cases} \tag{1.74}$$

and:

$$\begin{cases} s \cdot \hat{i}_d = -\frac{R}{L} \cdot \hat{i}_d + \omega_e \cdot \hat{i}_q + \frac{V_d}{L} \\ s \cdot \hat{i}_q = -\omega_e \cdot \hat{i}_d - \frac{\omega_e \cdot \lambda_{m,d}}{L} - \frac{R}{L} \cdot \hat{i}_q + \frac{V_q}{L} \end{cases} \tag{1.75}$$

For convenience some mathematical processing has to be done, first of all, the same factor $\frac{R}{L} \cdot \frac{\lambda_{m,d}}{L}$ is added and subtracted from the first equation of (1.75) to rewrite it in a more practical matrix:

$$\begin{cases} s \cdot \hat{i}_d = -\frac{R}{L} \cdot \hat{i}_d - \frac{R}{L} \cdot \frac{\lambda_{m,d}}{L} + \omega_e \cdot \hat{i}_q + \frac{V_d}{L} + \frac{1}{L} \cdot \frac{R}{L} \cdot \lambda_{m,d} \\ s \cdot \hat{i}_q = -\omega_e \cdot \hat{i}_d - \frac{\omega_e \cdot \lambda_{m,d}}{L} - \frac{R}{L} \cdot \hat{i}_q + \frac{V_q}{L} \end{cases} \tag{1.76}$$

$$s \cdot \begin{bmatrix} \hat{i}_d \\ \hat{i}_q \end{bmatrix} = \begin{bmatrix} -\frac{R}{L} & \omega_e \\ -\omega_e & -\frac{R}{L} \end{bmatrix} \cdot \begin{bmatrix} \hat{i}_d + \frac{\lambda_{m,d}}{L} \\ \hat{i}_q \end{bmatrix} + \frac{1}{L} \cdot \begin{bmatrix} v_d + \frac{R}{L} \cdot \lambda_{m,d} \\ v_q \end{bmatrix} \tag{1.77}$$

To express the adaptive model in a state space form, the factor $\frac{\lambda_{m,d}}{L}$ has been added to the first row of (1.77), that term has no influence on the mathematical result of the matrices because the derivative of a constant magnetic flux coming from the magnet is zero, but this is a first step that allows the matrix to be rewritten in state space.

$$s \cdot \begin{bmatrix} \hat{i}_d + \frac{\lambda_{m,d}}{L} \\ \hat{i}_q \end{bmatrix} = \begin{bmatrix} -\frac{R}{L} & \omega_e \\ -\omega_e & -\frac{R}{L} \end{bmatrix} \cdot \begin{bmatrix} \hat{i}_d + \frac{\lambda_{m,d}}{L} \\ \hat{i}_q \end{bmatrix} + \frac{1}{L} \cdot \begin{bmatrix} v_d + \frac{R}{L} \cdot \lambda_{m,d} \\ v_q \end{bmatrix} \tag{1.78}$$

Introducing some ad hoc fictitious variables $\hat{i}_d^{'} = \hat{i}_d + \lambda_{m,d}/L$, $\hat{i}_q^{'} = \hat{i}_q$, $v_d^{'} = v_d + \lambda_{m,d} R/L$, $v_q^{'} = v_q$, then:

$$s \cdot \begin{bmatrix} \hat{i}'_d \\ \hat{i}'_q \end{bmatrix} = \begin{bmatrix} -\frac{R}{L} & \omega_e \\ -\omega_e & -\frac{R}{L} \end{bmatrix} \cdot \begin{bmatrix} \hat{i}'_d \\ \hat{i}'_q \end{bmatrix} + \frac{1}{L} \cdot \begin{bmatrix} v'_d \\ v'_q \end{bmatrix} \tag{1.79}$$

So, to calculate the solution of i_d and i_q, we should solve the two differential equations in (1.78) but it can be difficult to do by a firmware running in a microcontroller with some computational constraints, so under the hypothesis of current slope changing very slowly with respect to the sampling frequency, it is possible to transform (1.78) from implicit to explicit form, committing deliberately the mathematical incorrectness of considering the explicit current at first part to be found at the current sampling instant (n), instead for all the implicit currents on the right we use values delayed by one sample (n-1). From (1.78):

$$\begin{cases} s \cdot \hat{i}_d^n = -\frac{R}{L} \cdot \hat{i}_d^{n-1} + \hat{\omega}_e^n \cdot \hat{i}_q^{n-1} + \frac{V_d^n}{L} - s \cdot \frac{\lambda_{m,d}}{L} \\ s \cdot \hat{i}_q^n = -\hat{\omega}_e^n \cdot \hat{i}_d^{n-1} - \frac{\hat{\omega}_e^n \cdot \lambda_{m,d}}{L} - \frac{R}{L} \cdot \hat{i}_q^{n-1} + \frac{V_q^n}{L} \end{cases} \tag{1.80}$$

After that, integration can be applied so as to obtain the estimated value of currents:

$$\begin{cases} \hat{i}_d = \int_{-\inf}^{t} [-\frac{R}{L} \cdot \hat{i}_d + \hat{\omega}_e \cdot \hat{i}_q + \frac{V_d}{L}] d\varepsilon - \frac{\lambda_{m,d}}{L} + c \\ \hat{i}_q = \int_{-\inf}^{t} [-\hat{\omega}_e \cdot \hat{i}_d - \frac{\hat{\omega}_e \cdot \lambda_{m,d}}{L} - \frac{R}{L} \cdot \hat{i}_q + \frac{V_q}{L}] d\varepsilon + c \end{cases} \tag{1.81}$$

Due to the sampled nature of the system, integration has been implemented in a discrete form; due to the computational limitations cited above, a simple forward Euler approximation has been used that offers a good functionality to complexity compromise considering the signal to be integrated as a slow variable. The starting point is an equation of this type:

$$\frac{dy}{dt} = a \cdot x(t) + b + \frac{dz}{dt} \tag{1.82}$$

Integrating the whole, results in an integrative term that contains all contributions of integrative memory and an instant term without memory:

$$y(t) = \int_{-\inf}^{t} [a \cdot x(\varepsilon) + b] d\varepsilon + z(t) \tag{1.83}$$

The control is carried out with a digital system and then each variable is sampled over time, so the continuous-time equation needs to be converted to a discrete-time equation considering that the integral degenerates into a mathematical summation. Having chosen the Euler method with forward approximation, between a sampling instant (n-1) and the next one (n), the continuous function degenerates in a constant whose value, for the whole sample time, is the value assumed by the function at the (n-1) sampling time. The content of each summation factor is the area of a rectangle with a base length equivalent to the sample time T_s while the height is equal to the constant value identified for approximating the function.

$$y(n \cdot T_s) = \sum_{\varepsilon=1}^{n} [a \cdot x(\varepsilon) + b] \cdot T_s + z(n \cdot T_s) \tag{1.84}$$

The value at a certain sample n is subdivided into:

- Old memory contribution containing the partial sums of the areas under the function until the $(n-1)$ sample.

$$y^{[n-1]} = \sum_{\varepsilon=1}^{n-1} [a \cdot x(\varepsilon) + b] \cdot T_s \tag{1.85}$$

- Instantaneous memory contribution containing the value of the area under the function contained between the $(n-1)$ and (n) samples.

$$T_s \cdot [a \cdot x^{[n]} + b] \tag{1.86}$$

- Contribution without memory at (n) sample that is only taken into account as an instantaneous value that is not accumulated at each cycle.

$$z^{[n]} = z(n \cdot T_s) \tag{1.87}$$

$$y^{[n]} = y^{[n-1]} + T_s \cdot [a \cdot x^{[n]} + b] + z^{[n]} \tag{1.88}$$

Starting from (1.81), the estimated currents calculation becomes:

$$i_d(n \cdot T_s) = \sum_{\varepsilon=1}^{n} [-\frac{R}{L} \cdot \hat{i}_d + \hat{\omega}_e \cdot \hat{i}_q + \frac{V_d}{L}] \cdot T_s - \frac{\lambda_{m,d}}{L} \tag{1.89}$$

- Old memory

$$i^{[n-1]}_{d\_old\_mem} = \sum_{\varepsilon=1}^{n-1} [-\frac{R}{L} \cdot \hat{i}_d + \hat{\omega}_e \cdot \hat{i}_q + \frac{V_d}{L}] \cdot T_s \tag{1.90}$$

- Instantaneous memory

$$i^{[n]}_{d\_istant\_mem} = T_s \cdot [-\frac{R}{L} \cdot \hat{i}_d + \hat{\omega}_e \cdot \hat{i}_q + \frac{V_d}{L}] \tag{1.91}$$

- No memory

$$i^{[n]}_{d\_no\_mem} = -\frac{\lambda_{m,d}}{L} \tag{1.92}$$

$$i_q(n \cdot T_s) = \sum_{\varepsilon=1}^{n} [-\hat{\omega}_e \cdot \hat{i}_d - \frac{\hat{\omega}_e \cdot \lambda_{m,d}}{L} - \frac{R}{L} \cdot \hat{i}_q + \frac{V_q}{L}] \cdot T_s \tag{1.93}$$

- Old memory

$$i^{[n-1]}_{q\_old\_mem} = \sum_{\varepsilon=1}^{n-1} [-\hat{\omega}_e \cdot \hat{i}_d - \frac{\hat{\omega}_e \cdot \lambda_{m,d}}{L} - \frac{R}{L} \cdot \hat{i}_q + \frac{V_q}{L}] \cdot T_s \tag{1.94}$$

- Instantaneous memory

$$i^{[n]}_{q\_istant\_mem} = T_s \cdot [-\hat{\omega}_e \cdot \hat{i}_d - \frac{\hat{\omega}_e \cdot \lambda_{m,d}}{L} - \frac{R}{L} \cdot \hat{i}_q + \frac{V_q}{L}] \tag{1.95}$$

- No memory

$$i^{[n]}_{q\_no\_mem} = 0 \tag{1.96}$$

The firmware code is:

```
for each sample time $T_s = 100\,\mu s$ do

    $i_{d\_istant\_mem} = T_s \cdot [-\frac{R}{L} \cdot \hat{i}_{d\_old} + \hat{\omega}_e \cdot \hat{i}_{qold} + \frac{V_d}{L}]$;
    $i_{d\_old\_mem} = i_{d\_old\_mem} + i_{d\_istant\_mem}$;
    $i_{d\_no\_mem} = -\frac{\lambda_{m,d}}{L}$;
    $i_{d\_actual} = i_{d\_old\_mem} + i_{d\_no\_mem}$;

    $i_{q\_istant\_mem} = T_s \cdot [-\hat{\omega}_e \cdot \hat{i}_{d\_old} - \frac{\hat{\omega}_e \cdot \lambda_{m,d}}{L} - \frac{R}{L} \cdot \hat{i}_{q\_old} + \frac{V_q}{L}]$;
    $i_{q\_old\_mem} = i_{q\_old\_mem} + i_{q\_istant\_mem}$;
    $i_{q\_no\_mem} = 0$;
    $i_{q\_actual} = i_{d\_old\_mem} + i_{q\_no\_mem}$;

    $i_{d\_old} = i_{d\_actual}$;
    $i_{q\_old} = i_{q\_actual}$;
end for
```

For the electrical speed information it is necessary to elaborate real and estimated currents with the adaptive law and PI regulator:

$$\omega_e = (K_p + \frac{K_i}{s}) \cdot (i_d \cdot \hat{i}_q - i_q \cdot \hat{i}_d - \frac{\lambda_{m,d}}{L} \cdot (i_q - \hat{i}_q)) \tag{1.97}$$

The discretized integral of the electrical speed has been used for the position information:

$$actual\_angle = actual\_angle + T_s \cdot \omega_e;$$

As mentioned in the section 1.2.3 about control with the sensor, there is the need of obtaining a normalized position variable with a sawtooth shape between -1 to 1 in order to feed the sine and cosine function used for Park matrix, but in that case the position information comes from a discretized integral so the wrapping need to be done via firmware, considering *actual_angle* the position elaborated by the sensorless algorithm and *actual_angle_normalized* the position wrapped between $-\pi$ rad to $+\pi$ rad,

```
if $actual\_angle \geq \pi$ then
    $actual\_angle = actual\_angle - 2 \cdot \pi$
else if $actual\_angle \leq \pi$ then
    $actual\_angle = actual\_angle + 2 \cdot \pi$
end if
$actual\_angle\_normalized = \frac{actual\_angle}{\pi}$
```

1.2.5 Motor control architecture

The main control is based on a state machine architecture to ensure the correct and safe operation of the motor.

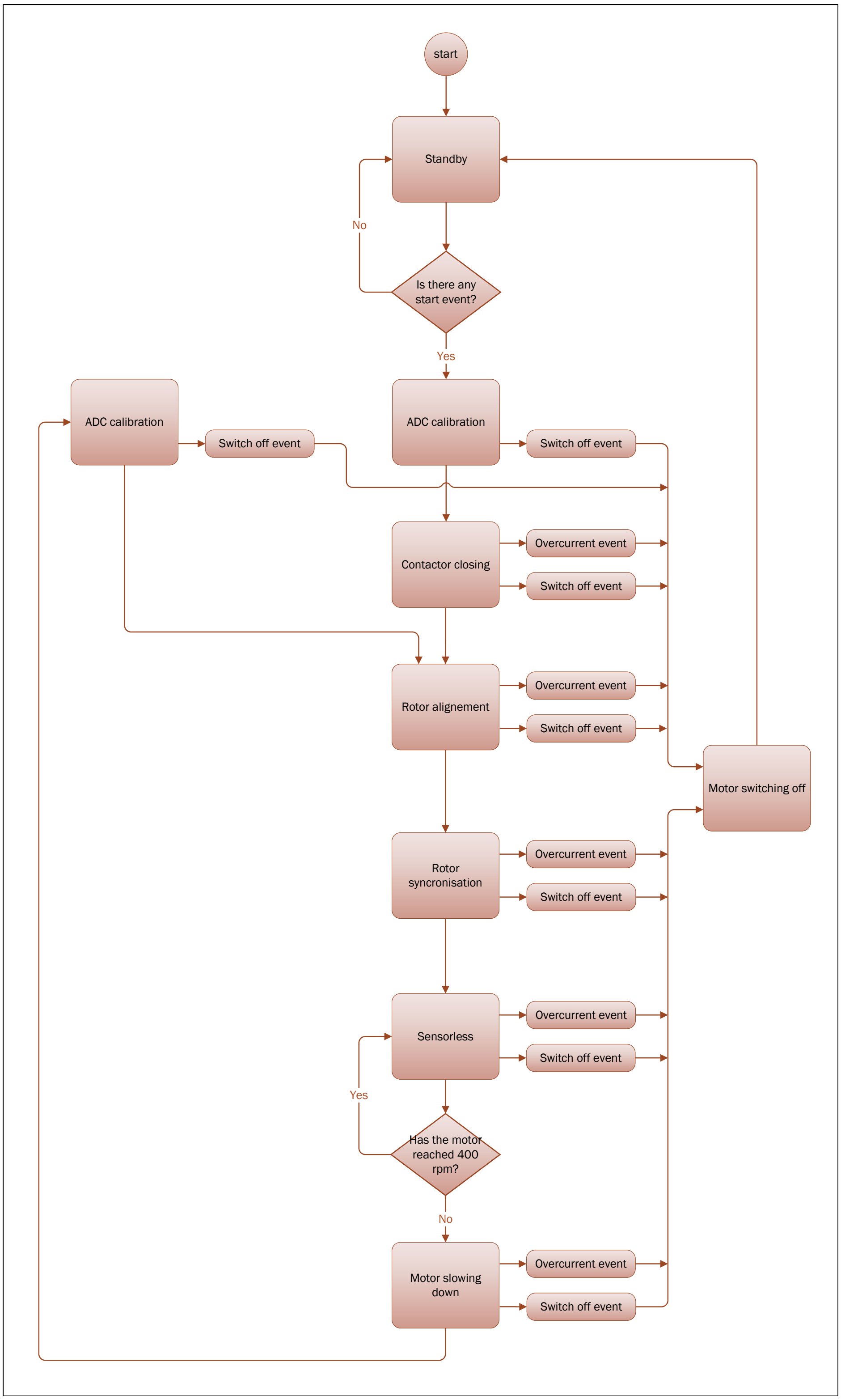

Figure 1.29: Block diagram of the motor control firmware

- Case STANDBY
  Is a standby block, where the firmware waits for a starting command from a user button or from an Electronic Controller Unit (ECU) command.

- Case ADC CALIBRATION
  Before powering up the three-phase inverter, it's necessary to calibrate the electronic circuitry for the current shunt and V_{bus} amplification. 100 samples are averaged for each channel in order to have an error constant to be subtracted from the current conversion during the motor control.
  - If a start-stop command is detected the state is changed in MOTOR SWITCHING OFF

- Case CONTACTOR CLOSING
  Before enabling the devices of the three-phase inverter it is necessary to send the closing command to the electromechanical safety contactor; considering its large size with a current rating of 250 A it takes a long time to close, up to 200 ms. If the contactor was closed at the same time as the inverter devices with instantaneous operation of the current loops, there would obviously be a very high current error on the d and q axes since no current could flow over the shunt and, consequently, the control would set the modulation indices of the motor phases to a very high value in order to require the desired current, but at the moment of physical closure of the contactor there would be an instantaneous overcurrent for the first cycles of control before it can take action to lower the indices.
  - In case of overcurrent detection the state is changed in MOTOR SWITCHING OFF
  - If a start-stop command is detected the state is changed in MOTOR SWITCHING OFF

- Case ROTOR ALIGNMENT
  As explained in (1.70) and (1.73), during the operation of the motor control

there is a need to always keep the rotor field aligned along the d-axis, thanks to the Park matrix providing current only on the q-axis it will be able to always hold the magnetic q-axis in advance of 90 electric degrees relative the d-axis, then the motor will work at maximum efficiency and torque density.

To do that only in this initial step of the state machine, for a few seconds a current is set on the d-axis by forcing a fixed angle into the Park matrix so as to allow the mechanical alignment of the rotor along this magnetic axis. Once this configuration is obtained, the current position is considered as the starting angle. To avoid possible situations of rotor stuck due to the rotor randomly aligned in counter phase with respect to the field on the d-axis and therefore unable to rotate and align correctly, two different angles are set 3 seconds apart to be sure to unlock a possible stuck rotor, then for convenience, a 30 degrees and 0 degrees angles are set.

  - In case of overcurrent detection the state is changed in MOTOR SWITCHING OFF
  - If a start-stop command is detected the state is changed in MOTOR SWITCHING OFF

- Case ROTOR SYNCRONISATION
  This state is concerned with the start of motor rotation. It is not possible to start the motor directly with the sensorless algorithm because it uses the reading of the back electromotive forces generated on the stator due to the rotation of the magnets, but at low speeds, they are negligible due to the low signal-to-noise ratio. It is necessary then to drive the start of the motor generating a fictitious angle via firmware that increases its rotational speed progressively until reaching a constant speed considered a priori reliable to attempt the on-fly switch to the sensorless algorithm. During that spinning up, the control is running in a condition of low performance and low torque density because it is not a field-oriented control by the way that the angle that is inserted into the Park matrix does not come from the control feedback block but is a fictitious one assuming that the rotor will be able to follow the angle. In this state, the

angle acceleration is performed with a certain profile and direction according to the direction request by the user in order to be ready at the moment of the control loop closing in the next state.

  - If a change of direction is required, the state is changed to MOTOR SLOWING DOWN
  - In case of zero speed request the state becomes MOTOR SWITCHING OFF
  - In case of overcurrent detection the state is changed in MOTOR SWITCHING OFF
  - If a start-stop command is detected the state is changed in MOTOR SWITCHING OFF

- Case SENSORLESS
  It is the main program for normal operation in sensorless mode. As soon as the acceleration of the motor in open loop mode is finished, the program instantly goes into this state where there are a series of controls and delicate actions.
  - First, after appropriate adjustments, the instantaneous position reached by the open loop motor is copied and pasted into the sensorless variables, enabling the driving of the Park matrix by the algorithm itself and closing the speed loop with the estimated speed.
  - The estimated speed is analyzed to ensure it is consistent with the minimum accepted values; in this case, the motor is considered properly started and synchronized with the sensorless algorithm or, otherwise, if the motor has lost the synchronization, the state is changed into MOTOR SLOWING DOWN.
  - The acceleration ramps are managed according to the speed required by the user and even the inversion of direction with an automatic management of the entire restart process.

  - In order not to make the overcurrent protection kick in, the values of the proportional and integrative constant and the output saturations of the current PI regulators are gradually modified in 4 steps every 100 ms.
  - In addition, there is an algorithm able to appropriately modify the braking output saturation values of the current PI regulators according to the direction of rotation to avoid a possible too hard braking of the motor that could cause an overvoltage on the DC bus of the inverter that in case of non-regenerative DC source or in absence of braking resistor can lead to a non-reversible failure of the inverter.
  - If a change of direction is required, the state is changed to MOTOR SLOWING DOWN
  - In case of zero speed request the state becomes MOTOR SWITCHING OFF.
  - In case of overcurrent detection the state is changed in MOTOR SWITCHING OFF
  - If a start or stop command is detected the state is changed in MOTOR SWITCHING OFF

- Case MOTOR SLOWING DOWN
  It is a timing frame to wait for an eventual slowing down of the motor before the automatic restart of the entire process.

  - after the slowing down time has elapsed there is a change of state to the ADC CALIBRATION
  - If a start or stop command is detected the state is changed in MOTOR SWITCHING OFF

- Case MOTOR SWITCHING OFF
  It is a timing frame for an eventual slowing down of the motor before passing to the STANDBY CASE.

A particular that deserves to be described is a problem that emerged in the first hardware version of the inverter, in detail during the transition from open-loop control to closed-loop control for sensorless look-up, which is a critical moment of the control, it was generating some impulsive disturbance on the phase currents and due to possible problems of the PCB tracks layout, there was some radiated emission on the microcontroller that were able to freeze it or move the input multiplexer of the ADC capacitor to an incorrect channel, making the current readings unusable, suddenly and dangerously stalling the motor. Before we had the second more efficient and reliable prototype it was necessary to find a way that could quickly notice the malfunction of the ADC and reboot them as recommended by the errata-sheet of the microcontroller. The algorithm is based on the recognition in the current values arrays at consecutive sampling times of at least one frame of equal values by use of a mobile window filter of 5 elements length, to switch off and on the ADC peripherals. At first, the usual way of using the Hardware Abstraction Layer (HAL) libraries was tried, but unfortunately, the libraries took 5 µs for each operation, which rendered the system unusable due to the large number of ADC failures happening. The switching on-off drivers have been rewritten directly accessing the memory-mapped registers in order to shorten on-off down to 0.5 µs.

1.2.6 Results

The third inverter and motor prototypes were delivered to the company and are currently in operation. The following pages report the characterization curves of the third prototype. To calculate the efficiency of the inverter, the ratio between the power on the three-phase line of the motor and the power absorbed by the DC bus was considered. For the motor efficiency, on the other hand, the ratio between the power transferred to the shaft and the power on the three-phase line was used.

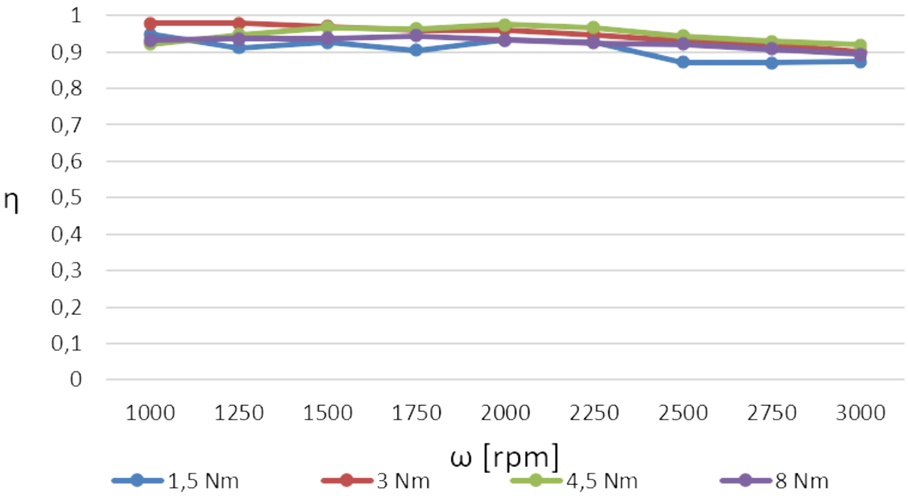

Figure 1.30: Inverter normalized efficiency

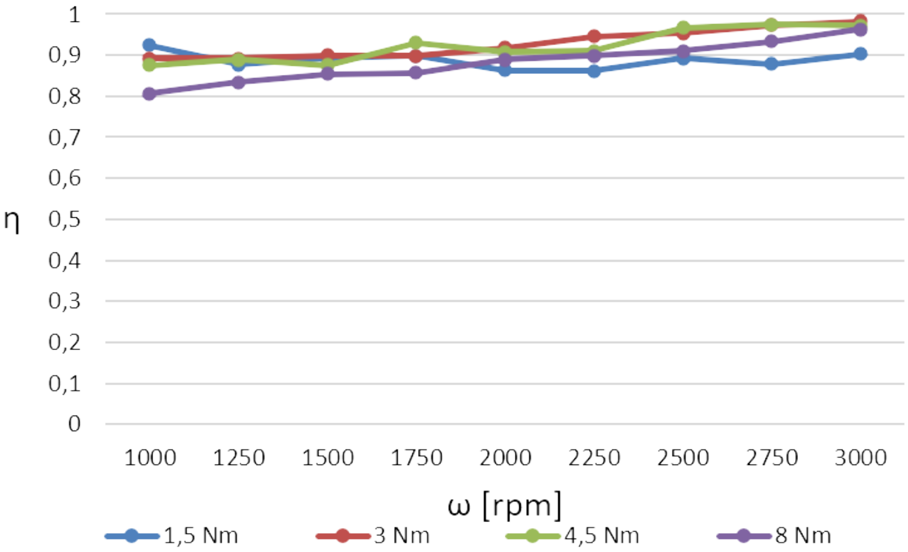

Figure 1.31: Motor normalized efficiency

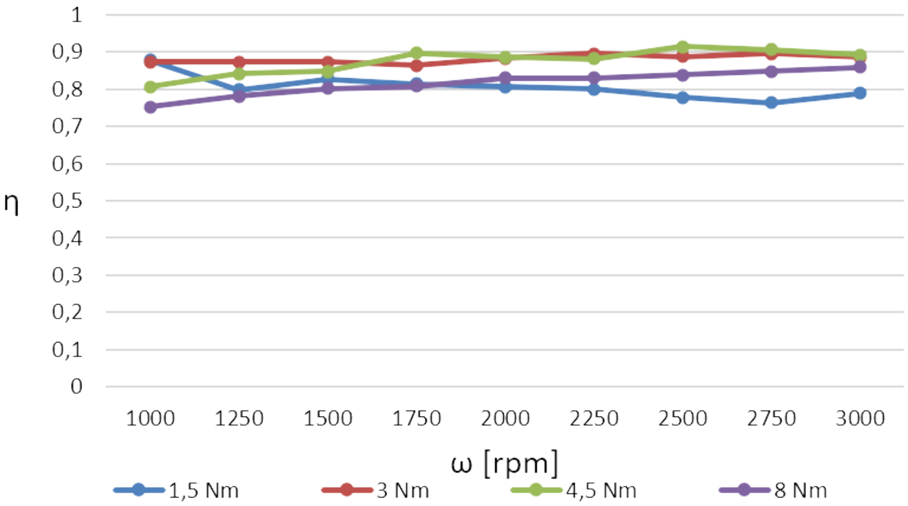

Figure 1.32: Total normalized efficiency

1.3 Active noise reduction

The rising use of electric motors in both industrial and domestic settings calls for a reduction in vibration and noise levels, which would enhance user comfort and improve system performance. Noise and Vibration Harshness (NVH) in electric motors can be divided into electromagnetic, mechanical, and aerodynamic sources [3]. Aerodynamic NVH is primarily caused by fans or airflow turbulence within the motor's air gaps. At higher speeds, these aerodynamic forces can create vibrations in the stator and motor housing, leading to high-frequency noise [4]. Mechanical NVH can arise from issues such as shaft misalignment, rotor imbalance, and mechanical elements like bearings, couplings, and gearboxes; the frequency ranges and intensity of mechanical NVH vary depending on the specific circumstances [5]. For instance, in a direct-drive system, the torque ripple generated by the motor directly affects the load, potentially degrading machine performance or damaging components[6]. Periodic disturbances caused by magnetic anisotropy, due to the slotted design of the stator, lead to fluctuations in torque and speed, which can adversely affect operation. By minimizing harmonic components and power fluctuations transmitted from the motor to the mechanical transmission system, overall performance and component lifespan can be greatly enhanced. Numerous mechanical engineering studies have focused on developing effective strategies for mitigating and isolating motor-induced vibrations in mechanical and transmission systems. These strategies can be classified into two main types: passive mechanisms that reduce vibration transmission from the motor to the drivetrain, and active control algorithms aimed at mitigating motor-generated vibrations. This study specifically addresses electric drives, where it is recognized that unwanted frequency components in the supply current spectrum negatively affect motor performance. Permanent magnet electric motors (PMEMs) produce torque ripples during operation, resulting in low-frequency components and mechanical vibrations that can adversely affect the powertrain and transmission. These vibrations are caused by parasitic torque arising from the interaction between the rotor's permanent magnets and the stator slots that contain the windings. This torque is influenced by the relative positioning of the stator and rotor, with its periodicity per revolution determined by both the number of magnetic poles and stator teeth. Torque ripple occurs throughout the motor's operating range, leading to jerky motion, especially at lower speeds. At higher speeds, the motor's inertia tends to mitigate the effects of vibrating torque on speed; however, torque ripple remains detrimental to the connected transmission chain, causing vibrations and acoustic noise.

“Passive” Vibration Reduction Techniques for limiting torque ripple are especially crucial for Interior Permanent Magnet Synchronous Motors (IPMSMs) and Surface Mount Permanent Magnet Synchronous Motors (SPMSMs). Various "passive" techniques can be implemented during the motor design phase to reduce the generation of torque ripple:

- Skewing stator or rotor magnets. This technique involves skewing the stator stack along its entire length at an angle equal to the slot pitch. It is highly effective in reducing torque ripple but it has the downside of raising production costs [7]. Similarly, rotor magnets can be skewed as well, which helps to reduce cogging torque with lower costs [8, 9].

- Fractional-Slot Concentrated-Winding (FSCW). Fragmenting the winding blocks of each pole into multiple stator cavities offers advantages such as high power density, a greater slot-filling factor, and reduced cogging torque [10, 11, 12, 13]. On the other hand, Integral Slot Concentrated Windings (ISCW) can be used as well, although they tend to exhibit a higher residual ripple [14].

- Stator dummy slots, slot bridges/slot openings. Auxiliary slots can be incorporated on select teeth and for a part of the stator length [15, 16]. To reduce the magnetic path differences experienced by the magnets, magnetic bridge connections (shoes) can be created between adjacent teeth, which helps minimize cogging torque [17]. Additionally, optimizing the ratio between the magnetic pole arc and pole pitch is essential for further reducing cogging torque [18]. However, one downside of slot bridging is flux leakage, which can lead to a decrease in average torque.

- Magnet pole geometry optimization. Research has demonstrated [19, 20] that adjusting the offset and shape of the magnets in a Surface Permanent Magnet Synchronous Motor can lead to a reduction in cogging torque.

- Stator geometry optimization. In [21] the relationship between the stator slot depth and the cogging torque has been examined, finding that a 6.7% increase in slot depth resulted in a 19.7% reduction in peak-to-peak cogging torque. Additionally, in [22] it has been demonstrated that modifying the thickness of the stator teeth and yoke can reduce vibration noise by increasing the resonant frequency, thereby enhancing the stiffness and stability of the stator core. Similar outcomes can also be observed in external rotor PMSMs [23].

- External rotor. In [18], the external rotor of a PMSM was designed to achieve the minimum cogging torque.

While all these techniques effectively mitigate cogging torque and vibrations through "passive" methods, they also complicate the motor’s construction and increase costs. As a result, these solutions are often impractical, especially for specialized motors or prototypes. Additionally, implementing these strategies can lead to a reduction in torque density and overall efficiency.

"Active" Vibration Control (AVC) systems are gaining more and more importance, especially for existing systems, since they can be installed without the need to replace any components, thus minimizing installation costs. In [24, 25], the torque ripple was reduced based on an analytical model. In [26], an iterative learning controller is used to minimize torque ripple, while in [27], an adaptive algorithm is used to self-tune the Fourier coefficients to minimize a periodic torque ripple. Many self-adaptive algorithms can be used with the aim of minimizing a cost function, be it noise, vibration, or torque ripple. In [28], the well-known Filtered-x Least Mean Square (FxLMS) [29] was used to dampen engine torque ripple, while in [30] the same algorithm was employed for the reduction of torque ripple in a PMSM.

1.3.1 New proposal of Active Vibration Control System

The active methods discussed are especially effective for small motors powered by converters that operate at high switching frequencies, resulting in a high cut-off frequency for the current loop. This setup allows for a sufficient frequency separation between the harmonics that need to be canceled and the cut-off frequency, enabling PI current regulators to effectively compensate for the magnetic anisotropy affecting the current set-points. If the bandwidth of the current regulator is inadequate to provide the required spectral components, the compensating signal should be applied directly to the d-q voltage axes.

In the proposed application [31], the motor has a nominal power of 3 kW with 72 stator teeth; therefore, the target frequency F_t to be canceled is the 72nd harmonic of the mechanical speed of the rotor F_r, i.e., F_t = 780 Hz for the 650 revolutions per minute (rpm) case (F_r = 10.8 Hz) and F_t = 960 Hz for the 800 rpm case (F_r = 13.3 Hz).

Since it is necessary to have a PWM frequency of at least one order of magnitude higher than the harmonic to be canceled to generate a sufficiently well-shaped sinusoid, and having a switching frequency of 10 kHz, the cut-off frequency of the current loop is limited to 700 Hz and the harmonic to be canceled is outside the bandwidth of the current controller. For this reason, unlike many studies that compensate for torque ripple by adding a specific signal to the current references, we investigated an alternative approach to attenuate the 72nd harmonic using a single-frequency feed-forward AVC that directly modifies the voltage applied to the d-axis. This method proves effective at frequencies above the current loop bandwidth and up to about an order of magnitude lower than the switching frequency, allowing for the cancellation of harmonics up to approximately 1 kHz. This technique is particularly applicable for reducing parasitic vibrations in manually operated tools and machinery, which fall under hand-arm exposure regulations. The ISO 5349-1:2001 standard, titled “Mechanical vibration Measurement and evaluation of human exposure to hand transmitted vibration,” specifically addresses the adverse effects of vibrations transmitted to the hands within the frequency range of 8 Hz to 1 kHz. The motor under test was installed on a motor test bench and monitored using a piezoelectric accelerometer along with three current sensors. Various combinations of amplitude and phase values for the injected current were evaluated to optimize the attenuation of the 72nd harmonic. Significant reductions in measured acceleration were achieved: -13.5 dB at 780 Hz when the motor operated at 650 revolutions per minute (rpm), and -29.0 dB at 960 Hz with the motor running at 800 rpm.

For the harmonic attenuation algorithm (Fig. 1.33), the cancellation signal is directly added to the voltage modulation index on the q-axis. The PI current regulator has been bypassed since, as mentioned earlier, the harmonic that needs to be canceled is outside its bandwidth. The injected current i''_q is a function of:

$$V''q = V_q + V_o \tag{1.98}$$

where

$$V_o = K_{INJ} \cdot \sin\theta_{INJ} + \varphi_{INJ} \tag{1.99}$$

is an oscillating voltage component for compensating the 72nd harmonic (torque ripple due to magnetic anisotropy), θ_{INJ} is the mechanical angle of the rotor position (estimated by the observer) multiplied by 72, φ_{INJ} and K_{INJ} are the phase and the amplitude, respectively, determined to obtain the maximum harmonic cancellation. The injected current i''_q is responsible for the torque:

$$T'' = T + T_c \tag{1.100}$$

where T is the ideal torque (1.70) and T_c is a compensating torque, due to the oscillating component V_o of $V''q$. The values of φ_{INJ} and K_{INJ} must be finely tuned so that T_c, caused by the injected current i''_q, can generate a mechanical vibration having the same amplitude and opposite phase compared to the 72nd harmonic to be attenuated.

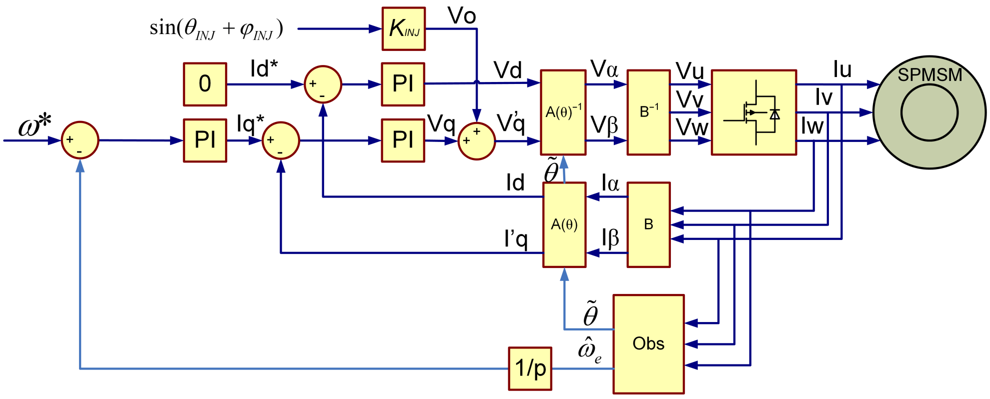

Figure 1.33: Control loop with current injection for active noise reduction

1.3.2 Active noise reduction feasibility simulation

Using the previously presented equations for the SPMSM model (1.67), the d-q control algorithm, and the proposed injection method, a MATLAB/Simulink simulation was carried out Fig. 1.34. With reference to Fig. 1.34, the electrical model of the motor is represented within the red block, surrounded by the d-q current control system. As discussed earlier, the i_d setpoint is maintained at zero, while the i_q is controlled by the speed loop. The compensation algorithm, applied in both the simulation and experimental phases, relies on two look-up tables (the MAG Look-Up Table and the PHASE Look-Up Table) that define the magnitude and angle of the compensating voltage sinusoid as functions of the rotating frequency. The values in these look-up tables were determined through linearization of the system around the operating point.

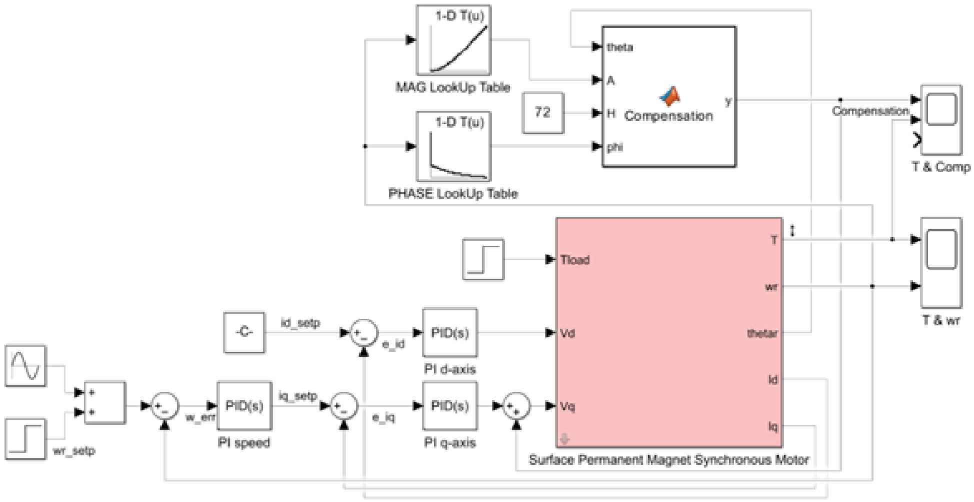

Figure 1.34: Simulink simulation for the automatic compensation of the noise based on the Look-Up table for phase and amplitude, generated by the inverse function transfer from current to torque.

The effectiveness of the proposed algorithm has been demonstrated through a plot of the motor torque, which compares the performance of the compensated system with that of the uncompensated system (Fig. 1.35).

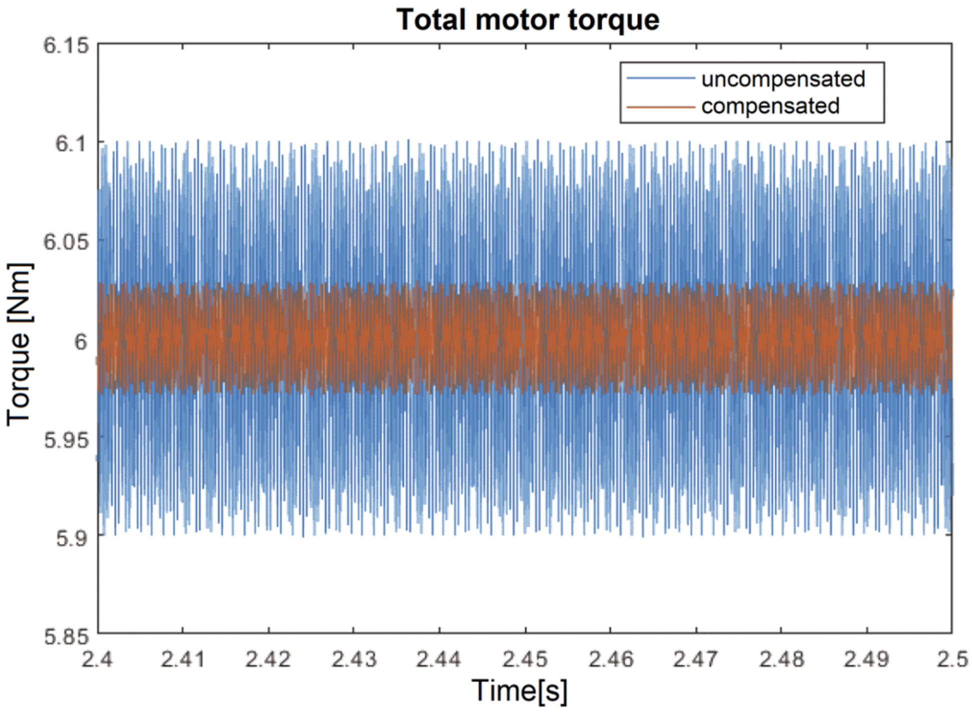

Figure 1.35: Output torque with and without compensation algorithm

As observed, the torque waveform using the compensation algorithm shows dampened oscillations, with only 0.42% of the drive torque compared to 1.7% without compensation. Following these promising simulation results, the compensation algorithm was then tested on an SPMSM mounted on a motor test bench.

1.3.3 Measurement System

The vibration and current signals were measured on the motor mounted on a motor test bench, as shown in Fig. 1.36.

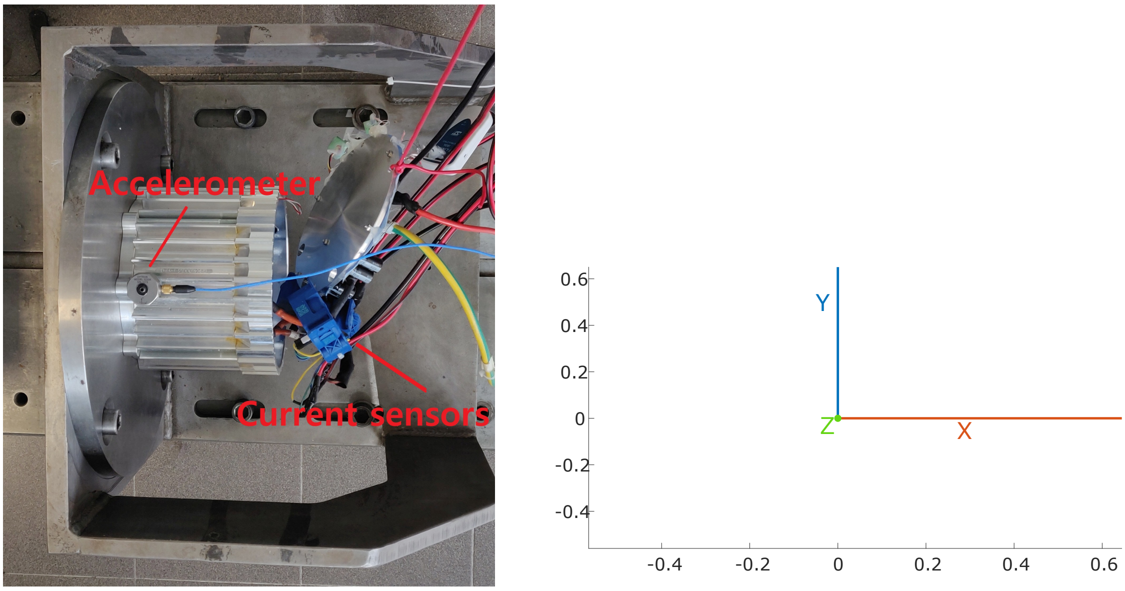

Figure 1.36: Accelerometer positioning on the motor and axes orientation

The vibration signals were acquired using a triaxial piezoelectric accelerometer, a Dytran model 3233A, whose specifications are shown in Table 1.4. At the same time, the three-phase currents were measured with current sensors, type LF 210-S from the manufacturer LEM. See Table 1.5 for LEM sensor specifications. An image and a schematic representation of the complete acquisition system are shown in Fig. 1.37.

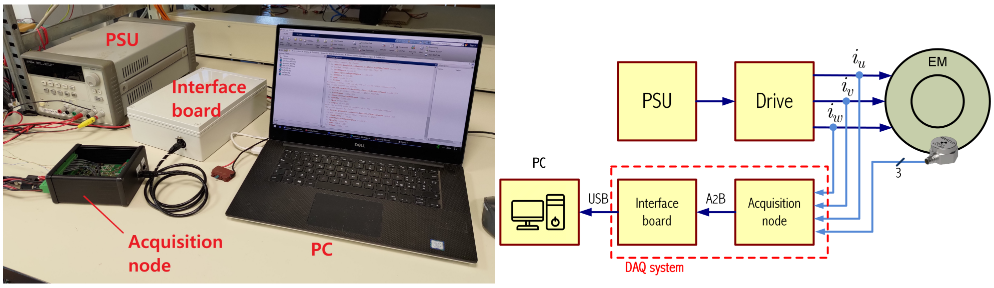

Figure 1.37: Electronic setup for analog signal adaptation and digital acquisition

Table 1.4: Dytran 3233A specifications

Specification	**Value**
Type	IEPE
Sensitivity	1000 mV/g
Measurement range	±5 g peak
Frequency range	X, Y: 0.4 Hz–6 kHz Z: 0.4 Hz–3 kHz
Maximum Output Voltage	±5 V
Excitation	18–30 V DC

Table 1.5: LEM LF 210-S specifications

Specification	**Value**
Primary current	200 A
Secondary current	100 mA
Nominal sensitivity	0.5 mA/A
Sensitivity error	±0.1%
Frequency bandwidth (-3 dB)	100 kHz
Supply voltage (nominal)	±15 V
Closed loop (compensated)	Yes

All of these signals were captured using a digital Data Acquisition (DAQ) system consisting of two components: an Interface Board (IB) and several Acquisition Nodes (AN) connected to the IB via the Automotive Audio Bus (A2B). Each network can transmit up to 32 signals, all synchronized by the bus with minimal jitter [32] and a deterministic latency of 50 µs, at a sampling frequency of 48 kHz over a single unshielded twisted pair wire.

1.3.4 Results

The experimental campaign was conducted at two different motor speeds, 650 rpm, a rotor frequency of F_r = 10.8 Hz, and 800 rpm, being F_r = 13.3 Hz. The motor was run at the target speed for 30 min to reach a stable temperature condition before starting the measurements. For each speed, a total of 25 measurements were performed by combining five values of amplitude and five values of phase of the injected current are shown in Table 1.6 and Table 1.7 with the aim of maximizing the cancellation effect.

Table 1.6: Vibration attenuation in function of current modulation index amplitude and phase values at 650 rpm

Modulation index (KINJ)	Phase (rad)=-1.05	Phase (rad)=-0.79	Phase (rad)=0	Phase (rad)=0.79	Phase (rad)=1.05
0.05	-7.5 dB	-10.0 dB	-7.5 dB	-1.0 dB	0 dB
0.06	-5.0 dB	-8.5 dB	-11.5 dB	-1.0 dB	0.5 dB
0.07	-5.0 dB	-8.0 dB	-13.5 dB	-1.5 dB	0 dB
0.08	0 dB	-2.0 dB	-9.0 dB	-1.0 dB	0.5 dB
0.09	1.5 dB	0 dB	-5.0 dB	-1.0 dB	1.0 dB

Table 1.7: Vibration attenuation in function of current modulation index amplitude and phase values at 800 rpm

Modulation index (KINJ)	Phase (rad)=-1.05	Phase (rad)=-0.79	Phase (rad)=0	Phase (rad)=0.79	Phase (rad)=1.05
0.05	-2.5 dB	-5.0 dB	-11.0 dB	-2.0 dB	0 dB
0.06	-1.5 dB	-4.0 dB	-17.5 dB	-2.5 dB	-0.5 dB
0.07	-0.5 dB	-3.0 dB	-29.0 dB	-2.0 dB	0 dB
0.08	1.5 dB	0 dB	-13.0 dB	-2.0 dB	0 dB
0.09	2.0 dB	0 dB	-8.0 dB	-2.0 dB	0 dB

The vibration level was first measured for the nominal condition of the motor, i.e., in thermal equilibrium, without current injection, along the Y direction (the orientation of the accelerometer can be seen in Fig. 1.36). This measurement was carried out to identify the target frequency F_t to be reduced in the interested operating frequency range. The spectra of acceleration levels were calculated by means of fast Fourier transform (FFT), averaging multiple blocks of 2^{16} samples each, overlapped by 75%, with Hann windowing. The frequency resolution is $d_f = f_s/2^{16} \simeq 0.73Hz$.

The spectra are referred to the acceleration reference unit of the I.S. for dB conversion; that is, $a_{ref} = 10^{-6} m/s^2$. The results are shown in Fig. 1.38 (left) for the 650 rpm case ($F_r \simeq 10.8Hz$) and in Fig. 1.39 (left) for the 800 rpm case ($F_r \simeq 13.3Hz$). The target frequency F_t, the one having the largest amplitude, resulted as the 72^{th} harmonic of the fundamental rotor frequency; that is, $F_t = 780Hz$ for the 650 rpm case and $F_t = 960Hz$ for the 800 rpm case. As can be seen in Fig. 1.38 (right) for the 650 rpm case and in Fig. 1.39 (right) for the 800 rpm case, the target frequencies F_t are also modulated by the rotor frequency F_r, which in turn causes the appearance of two further disturbance harmonics, i.e., the 71^{th} and the 73^{th}. They correspond to the frequencies $F_t^{'} = 769.2Hz$ and $F_t^{''} = 790.8Hz$ for the 650 rpm case and $F_t^{'} = 946.7Hz$ and $F_t^{''} = 973.3Hz$ for the 800 rpm case. However, only the 72nd harmonic was considered in this work, leaving a multi-tone cancellation algorithm for subsequent developments.

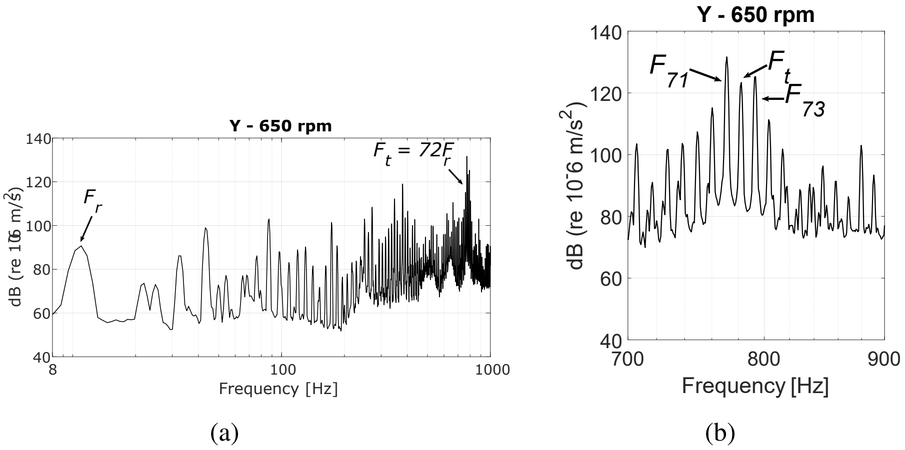

(a) (b)

Figure 1.38: ISO 5349-1:2001 standard for human exposure to hand-transmitted vibration inside 8 Hz to 1 kHz spectrum, and 72^{th} harmonic to be deleted, at the rotation speed of 650 [rpm]

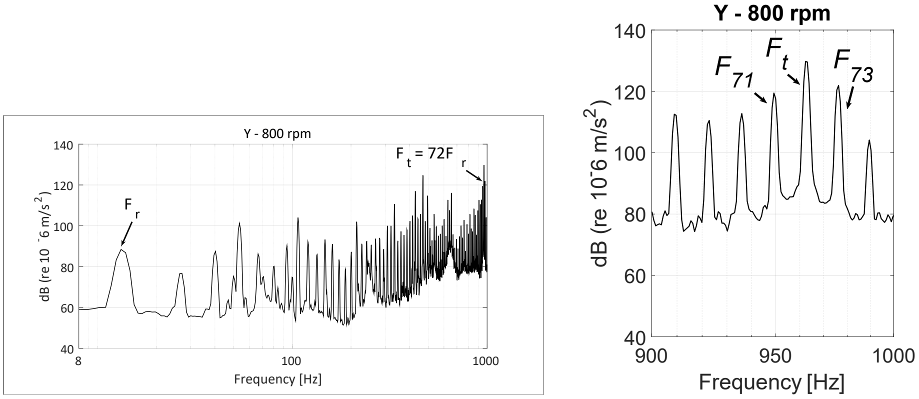

(a) (b)

Figure 1.39: ISO 5349-1:2001 standard for human exposure to hand-transmitted vibration inside 8 Hz to 1 kHz spectrum, and 72^{th} harmonic to be deleted, at the rotation speed of 800 [rpm]

The effectiveness of the current injection technique was evaluated by calculating the amount of reduction in terms of acceleration level (dB) at the target frequency F_t, for each of the 25 conditions as a function of phase and amplitude of the injected current. The minimum points in the charts of Fig. 1.40 correspond to the optimal combinations of phase and amplitude of the injected current, which provides the maximum cancellation performance. Remarkable results were obtained, with a reduction of the vibration level equal to -13.5 dB at $F_t = 780Hz$ for the 650 rpm case and to -29 dB at $F_t = 960Hz$ for the 800 rpm case. One can note that the optimal working point becomes narrower as the frequency increases, as usually happens in most of the Active Noise Cancelling (ANC) applications [33, 34].

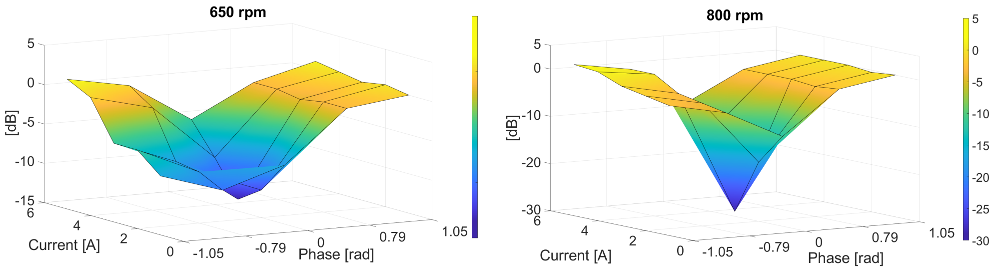

(a) (b)

Figure 1.40: Characterization of motor response to the current injection to find the best amplitude-phase combination for the best attenuation level for both 650 and 800 rpm cases.

Then, the spectra of the acceleration level were also calculated for the AVC-on condition, running with the optimal parameters for the injected current. In Fig. 1.41, they are shown in comparison with the nominal conditions, confirming the above analysis. One can note the target frequency F_t = 780 Hz for the 650 rpm case is reduced by 13.5 dB, and F_t = 960 Hz for the 800 rpm case by 29 dB. There is a significant reduction in noise, in the case of 650 rpm, there is a 78% reduction, while at 800 rpm, there is a reduction in noise of 96%.

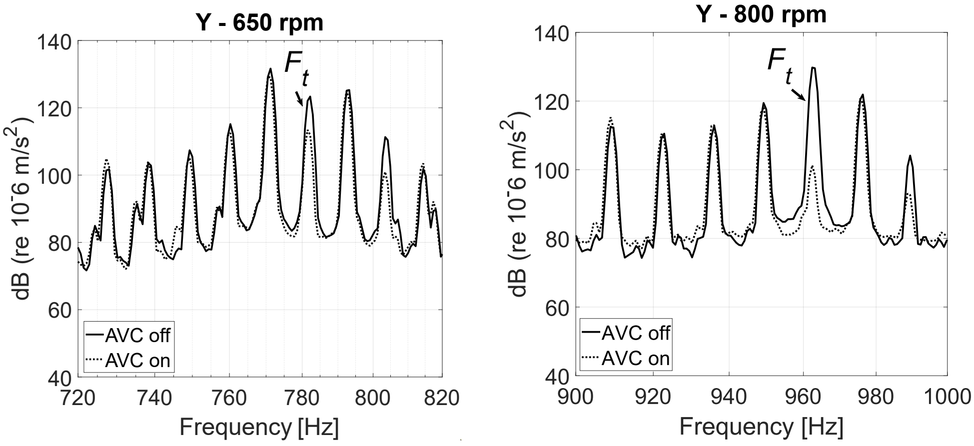

(a) (b)

Figure 1.41: Harmonic amplitude reduction due to AVC on for both 650 and 800 rpm cases

Eventually, the time domain signals were analyzed by means of their Root Mean Square (RMS) value. For each tested speed, the optimal condition with AVC on and the nominal condition with AVC-off were compared in Table 1.8, with the aim of assessing the amount of overall vibration level reduction in the frequency range 8 Hz – 1 kHz, considered by the hand-arm regulation for manually operated tools and machinery. The overall acceleration levels were reduced by 1.7 dB for the 650 rpm case and by 3.4 dB for the 800 rpm.

Table 1.8: Motor Speed and Overall Acceleration Levels

Motor Speed [rpm]	AVC System Condition	Overall Acceleration Level [dB]
650	OFF	77.2
650	ON	75.5
800	OFF	76.3
800	ON	72.9

Chapter 2

Test bench for "Arena del futuro" asphalt characterization

For recharging electric vehicles in motion, several options are available: an overhead pantograph system, a sliding contact system under the pavement, and a wireless energy transfer system from below the asphalt [35]. For safety and ease of use, the wireless system is the most promising. The company Brebemi has developed an experimental circuit "Arena del futuro" to test the recharging of cars and buses while in motion, near the Chiari East tool gate featured with a total length of 1,050 meters, a width of 8 meters, 7 types of pavement and composed by a huge amount of coil tuned to resonate at the frequency of 86.6 kHz and with a total absorbed power of 1 MW [36, 37].

The fundamental idea of this work was to experimentally investigate in the laboratory the effect of the magnetic field on various bituminous materials, which will ultimately form the layer of aggregate above the coils. Furthermore, this project aims to keep all options open for potential second-order effects that may arise, particularly the possibility of absorption/distortion of the magnetic field by the bitumen, especially as it may change over time due to factors such as oxidation of the bonds. To observe the relationship between field intensity and aging, we decided to position the samples at three different distances from the coil, allowing us to appreciate the attenuation of the field, considering that its intensity decreases quadratically with distance.

2.1 Hardware

2.1.1 Test bench

The test bench designed was intended to measure magnetic field intensity at various heights Fig. 2.1. It consists of three drywall shelves positioned above the coil (which rests on an additional shelf for fire safety), serving the dual purpose of a support platform for the samples and a support structure for the magnetic field sensors.

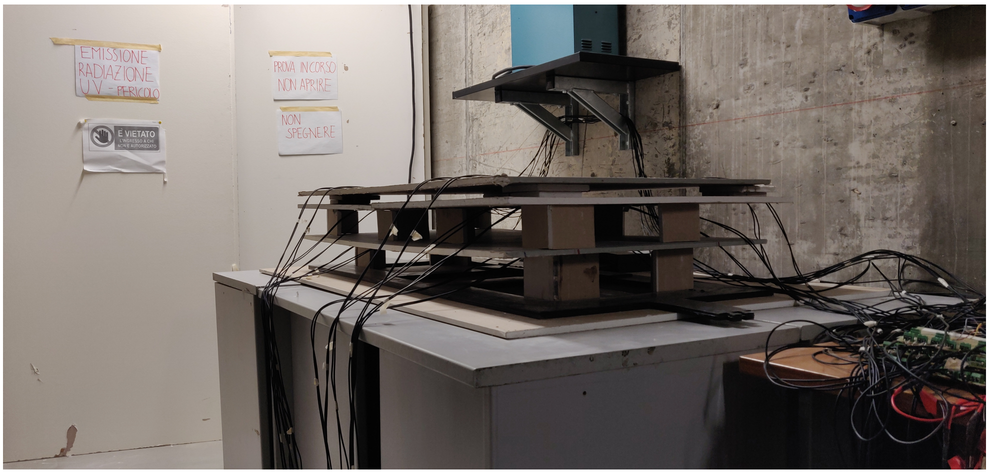

Figure 2.1: Test bench

- Level 0: The level on which the coil rests.
- Level 1: It is 10 cm above the coil, the first level for supporting samples, with sensors fixed on the underside of the shelf to obtain readings of the field just below the samples (undistorted by any samples).
- Level 2: It is 20 cm above the coil, the second level for samples, with sensors also fixed on the underside of the shelf to obtain readings of the field just below the samples.
- Level 3: It is 23 cm above the coil, the final shelf that completes the structure, serving solely to support sensors. In this case, the sensors were positioned on the

top side of the shelf, extending an additional 0.5 cm to facilitate measurements where the field would be more geometrically linear.

Each level from the first to the third was equipped with 8 sensors (corresponding to the positions of the samples), ensuring they were perfectly aligned with their homologous positions so that across the three Z-axis height values, the 8 sensors on each plane shared the same XY coordinates. To achieve this, reference marks were traced on all planes indicating where the sensor heads should be placed. It was essential to ensure that once the various shelves were mounted, the sensors at each level were precisely aligned.

To facilitate this, after taking all necessary measurements and marking the various references on the shelves, we decided to create reference templates by stacking all the shelves one atop the other without spacers. Meticulously, small holes were drilled with a 1.5 mm diameter bit at the four corners of each level. This way, once the structure was assembled, a thin wire could be passed from the top shelf down to the base, ending with a weight. By observing that the wire passed without ever touching the shelves, we were able to coordinate the measurements and ensure perfect alignment of the various levels.

To secure the sensors, and in order to avoid any solution involving metallic materials and not wanting to use adhesives that would complicate the replacement of faulty sensors, we opted for rectangular PVC pieces shaped with hot air Fig. 2.2. Once glued on one side, these pieces could, due to their elasticity, hold the sensors firmly in place against the drywall.

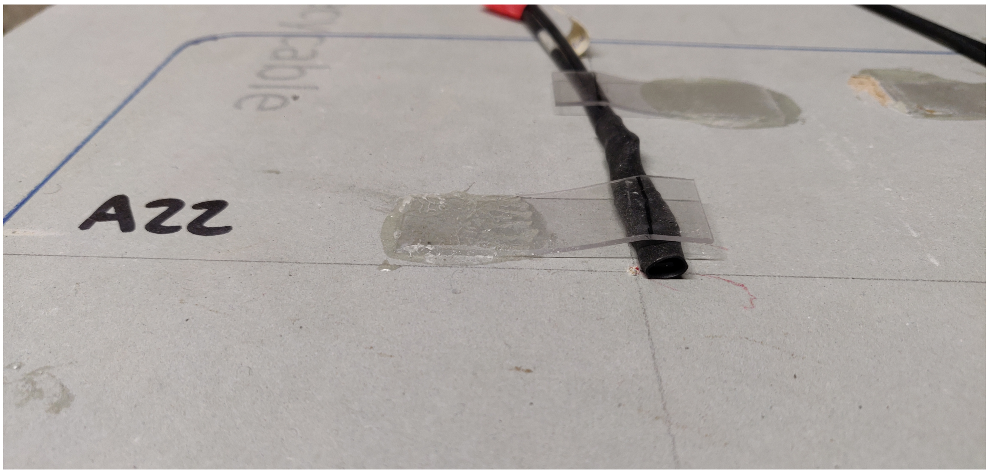

Figure 2.2: Sensor attachment

2.1.2 Sensors

For the measurement of the magnetic field, Hall effect sensors produced by Allegro were chosen. These sensors are powered by a 5 VDC supply voltage and have a measurement range of ±50 G (Gauss) or ±5 mT, with an analog output that takes the value of 0 V for -5 mT (-50G) measurement, 2.5 V for the absence of a magnetic field, and 5 V for 5 mT (50G) measurement. For clarity, the first-level sensors are numbered from 0 to 7, the second-level sensors from 10 to 17, and the third-level sensors from 20 to 27, so that, for example, sensors 4, 14, and 24 represent readings in the same XY plane but at three different heights along the Z axis. Fig. 2.3

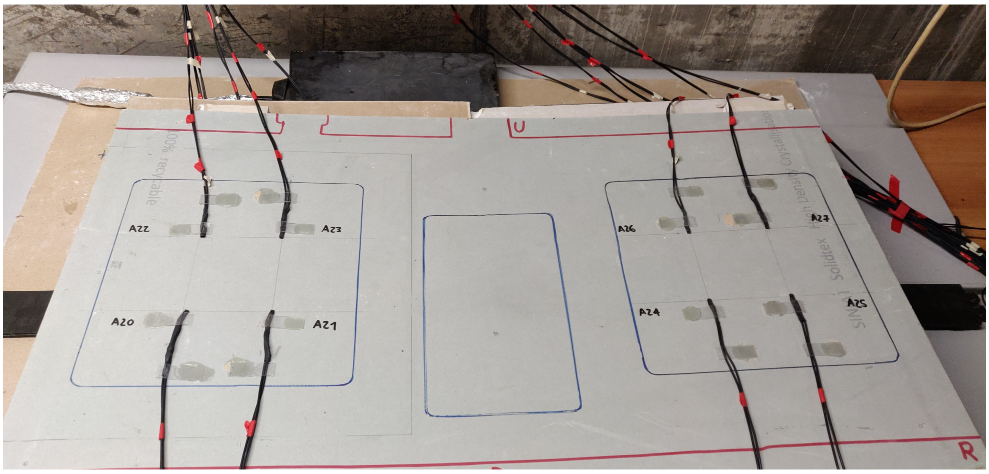

Figure 2.3: Sensors placements

2.1.3 Signals conditioning

The signal from the sensors had to be appropriately conditioned because if it has wanted to acquire the 24 sinusoidal magnetic field signals using a data acquisition board (National Instruments DAQ) that consists of a single analog-to-digital converter (ADC) with a sampling rate of 255 kS/s, we would obtain readings that are completely undersampled, because of the frequency of the magnetic coil being 86.6 kHz. Therefore, the solution is to transform each sinusoidal value into a continuous value representing the peak value. To achieve this, a peak detection front-end circuit Fig. 2.4 was created for each channel, allowing the National Instruments board to acquire continuous values.

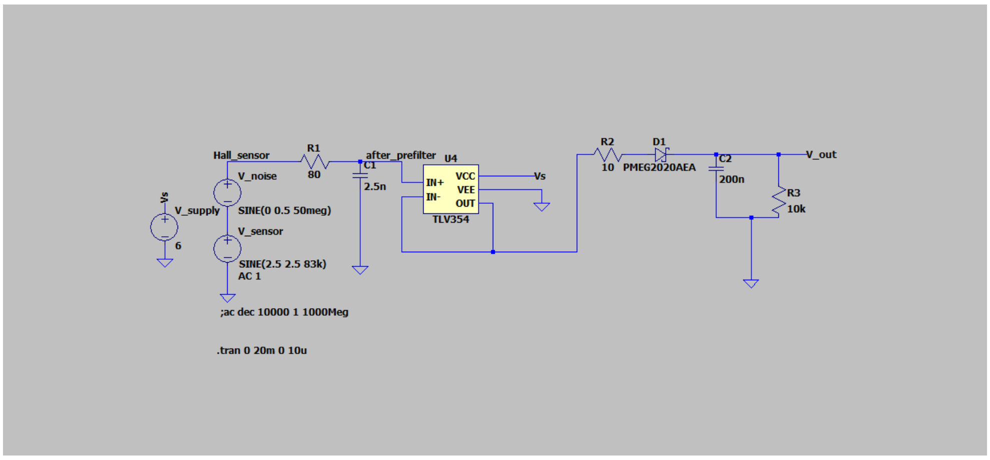

Figure 2.4: LTspice simulation of the peak revealing circuit

In particular, there is a first RC low-pass filtering stage to filter out any disturbances, with a cutoff frequency f_{3dB} (2.1) chosen to allow the useful signal to pass unchanged while blocking potential disturbances in the higher frequency bands. With $C_1 = 2.5\,\mathrm{nF}$ chosen, the value of R_1 (2.2) was selected by setting $f_{3dB_{in}} = 830\,\mathrm{kHz}$ ensuring it is greater than R_{min} (2.7) calculated at the operating frequency to avoid exceeding the maximum current rating $I_{max} = 10\,\mathrm{mA}$ coming from the sensor.

$$f_{3dB_{in}} = \frac{1}{2 \cdot \pi \cdot R_1 \cdot C_1} \tag{2.1}$$

$$R_1 = \frac{1}{2 \cdot \pi \cdot f_{3dB_{in}} \cdot C_1} = \frac{1}{2 \cdot \pi \cdot 830 \cdot 10^3 \cdot 2.5 \cdot 10^{-9}} = 76.7\,\Omega \tag{2.2}$$

$$Z_{C_1} = \frac{-j}{2 \cdot \pi \cdot f \cdot C_1} \tag{2.3}$$

$$X_{C_1} = \frac{1}{2 \cdot \pi \cdot f \cdot C_1} = \frac{1}{2 \cdot \pi \cdot 83 \cdot 10^3 \cdot 2.5 \cdot 10^{-9}} = 767\,\Omega \tag{2.4}$$

$$|R_{min} + Z_{C_1}| = \left| \frac{V_{max}}{I_{max}} \right| \tag{2.5}$$

$$|R_{min}+Z_{C_1}| = \sqrt{(\mathfrak{Re}(R_{min})+\mathfrak{Re}(Z_{C_1}))^2+(\mathfrak{Im}(R_{min})+\mathfrak{Im}(Z_{C_1}))^2} = \sqrt{R_{min}^2+X_{C_1}^2} \tag{2.6}$$

$$R_{min} = \sqrt{\frac{V_{max}^2}{I_{max}^2}-X_{C_1}^2} = \sqrt{\frac{5^2}{(10\cdot 10^{-3})^2}-767^2} \tag{2.7}$$

According to the capacitor value and (2.8), there is no minimum value of R_1

$$S = \nexists\, R_{min} \in \mathbb{R} \tag{2.8}$$

For the band regulation of the peak detector, C_2 and R_3 has been set choosing a 3 dB frequency $f_{3dB_{out}}$ significantly lower than the frequency of the input signal to eliminate residual ripple, and since the measurements are at very low dynamics, there is no risk of losing detail. $C_3 = 200\,\text{nF}$ has been chosen significantly big in order to avoid being affected by any potential leakage currents from the diode or its own, so R_2 becomes from (2.9)

$$R_2 = \frac{1}{2\cdot\pi\cdot f_{3dB_{out}}\cdot C_3} = \frac{1}{2\cdot\pi\cdot 83\cdot 200\cdot 10^{-9}} = 9.6\,\text{k}\Omega \tag{2.9}$$

A Schottky diode PMEG2020AEA has been chosen that for forward current of 10 mA has a threshold voltage of 200 mV.

A TLV354 op-amp buffer was included in an inverting configuration to decouple the input filter from the output filter; otherwise, it wouldn't have been possible to achieve the previously described calibrations. The characteristics that led to this choice include rail-to-rail levels for both input and output, as well as a high slew rate $SR = 150\,\text{V}/\mu\text{s}$, high output current around 100 mA useful for the cyclic fast charging of the output filter.

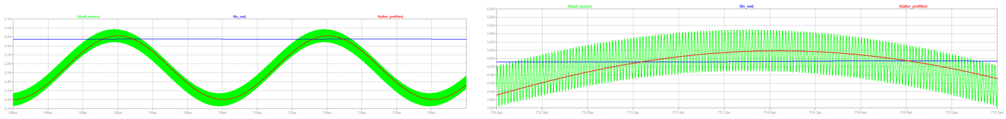

(a) (b)

Figure 2.5: Signal coming from the Hall sensor added with a sinusoidal disturbance in green, signal filtered for the sinusoidal disturbance elimination red, peak information to be fed into the digital acquisition card blue

2.2 Software

An entire software was developed in LabVIEW capable of recording all 24 signals simultaneously to a CSV file every 20 s. Specifically, for each channel, 100 readings per second are taken (conditioned by various correction coefficients to convert the information from voltage to Gauss), displayed on a time-based graph, and every 10 seconds, one packet of 100 readings is taken, averaged, and recorded in the file along with the corresponding date and time logs. The coil provided by Electreon and the driver designed by Politecnico di Milano is designed to conduct accelerated testing on asphalt, intermittently powering the coil to simulate continuous vehicle traffic (5 s on, 10 s off) with a frequency of 86.6 kHz. A control was added to the acquisition code to discard any packets if even a single sample of 100 was acquired during an "off" moment. To achieve this, a sentinel sensor (number 0) was chosen, and the code checks each cycle to see if every sample in the considered packet falls within an acceptable range or not. If the control passes, all packets from each channel are processed, averaged, and recorded; if not, they are all discarded, and the code retries in the next 10 s slot.

2.3 Results

The acquisition system has been calibrated and tested and can correctly detect and record the magnetic field of all sensors. The results about the behavior of asphalt aging under magnetic fields are not available yet because tests are still in progress.

Conclusion

The current period is leading to the development of technological maturity in an attempt to address problems that have been latent for years, specifically the issue of pollution caused by heavy-duty machinery or automotive vehicles. In particular, in collaboration with the company Casappa S.p.A, it was decided to begin a long and complex process of electrifying excavators, starting with the least critical actuator for the machine's functionality but most interesting from an engineering challenge perspective: the fan-drive for cooling the hydraulic oil in the machines. The challenge arises from: the high temperatures near the oil radiator, the wide speed dynamics, and the high compactness and reliability required when integrating the inverter into the brushless motor. First, a theoretical analysis was conducted with Simulink simulations of the entire electromechanical system, linearizing the fan and then implementing controls with various PI controller architectures with one and two degrees of freedom, comparing their ability to maintain speed at steady-state and in case of sudden torque insertion. It was observed that, as expected, the 2-degree-of-freedom architectures were much better at recovering speed in the event of a sudden torque insertion. In coordination with the company, evaluating the use case (i.e., torque applied as a function of speed and never suddenly), and considering computational resources of the microcontroller, it was decided to use the 1-degree-of-freedom PI controller, which provides an excellent performance to computational cost ratio.The inverter powered at 48 V, which was designed during my master's thesis in collaboration with the company, was first perfected. The entire firmware for vector control was designed and written, first with a speed sensor and then with a rotor position estimation algorithm to increase reliability. A test bench was set up to test the motor, and after three prototypes of inverters and motors, a very satisfactory result was achieved, with drive efficiency reaching up to 90%. During development, a very noisy motor was discovered due to cogging between rotor magnets and the stator caves. A solution was devised to reduce vibrations via firmware by injecting custom current components into the stator. As a result, there was a significant reduction in noise: for a noise frequency of 780 Hz (650 rpm) there was a reduction in noise by 13.5 dB, and for 960 Hz (800 rpm) there was a reduction in noise by 29 dB. The RMS overall vibration level in the frequency range of 8 Hz – 1 kHz, considered by hand-arm regulation for manually operated tools and machinery, was reduced by 1.7 dB for the 650 rpm case and by 3.4 dB for the 800 rpm. Finally, I collaborated on a project to create a test bench to conduct accelerated aging tests on asphalt samples to be used in an experimental circuit for wireless vehicle charging, to study the effects of the magnetic field at frequency of 86.6 kHz on various bituminous materials. The mechanical structure was prepared, the connections for various Hall effect sensors were made, along with the analog adaptation stages and peak detection of the sinusoidal magnetic signal. Finally, the code was written in LabVIEW for recording the data and subsequent graphing. The tests are still ongoing, and the data are being analyzed by the UNIPR civil engineering research team.

Bibliography

[1] Hidefumi Taguchi and Mituhiko Araki. Two-degree-of-freedom pid controllers — their functions and optimal tuning. *IFAC Proceedings Volumes*, 33(4):91–96, 2000. IFAC Workshop on Digital Control: Past, Present and Future of PID Control, Terrassa, Spain, 5-7 April 2000. URL: `https://www.sciencedirect.com/science/article/pii/S1474667017382265`, `doi:10.1016/S1474-6670(17)38226-5`.

[2] Jiaxin Wu, Hanpei Wei, Yi Zhang, and Haifeng Wei. Sensorless vector control of permanent magnet synchronous motor based on model reference adaptive system. In *2017 3rd IEEE International Conference on Computer and Communications (ICCC)*, pages 2879–2883, 2017. `doi:10.1109/CompComm.2017.8323058`.

[3] J.F. Gieras, C. Wang, and J. Cho Lai. *Noise of Polyphase Electric Motors*. CRC Press, Boca Raton, FL, USA, 1st edition, 2005.

[4] E. Król and M. Maciążek. Identification and analysis of noise sources of permanent magnet synchronous traction motor with interior permanent magnet. *Energies*, 16:6018, 2023. `doi:10.3390/en16166018`.

[5] K. Feng, J.C. Ji, Q. Ni, and M. Beer. A review of vibration-based gear wear monitoring and prediction techniques. *Mech. Syst. Signal Process.*, 182:109605, 2023. `doi:10.1016/j.ymssp.2022.109605`.

[6] Y. Chi, G. Shi, H. Guo, N. Yang, C. Zhu, and M. Cui. Design and performance investigation of a vehicle drive system with a 12/10 flux-switching permanent magnet motor. *Machines*, 10:1216, 2022. `doi:10.3390/machines10121216`.

[7] C. Bianchini, F. Immovilli, E. Lorenzani, A. Bellini, and M. Davoli. Review of design solutions for internal permanent-magnet machines cogging torque reduction. *IEEE Trans. Magn.*, 48:2685–2693, 2012. `doi:10.1109/TMAG.2012.2199509`.

[8] M. Aydin and M. Gulec. Reduction of cogging torque in double-rotor axial-flux permanent-magnet disk motors: A review of cost-effective magnet-skewing techniques with experimental verification. *IEEE Trans. Ind. Electron.*, 61:5025–5034, 2014. `doi:10.1109/TIE.2013.2276777`.

[9] R. Islam and A.P. Ortega. Practical aspects of implementing skew angle to reduce cogging torque for the mass-production of permanent magnet synchronous motors. In *Proceedings of the 2017 20th International Conference on Electrical Machines and Systems (ICEMS)*, pages 1–5, Sydney, Australia, 2017. IEEE. `doi:10.1109/ICEMS.2017.8056084`.

[10] A. El-Refaie. Fractional-slot concentrated-windings: A paradigm shift in electrical machines. In *Proceedings of the 2013 IEEE Workshop on Electrical Machines Design, Control and Diagnosis (WEMDCD)*, pages 24–32, Paris, France, 2013. IEEE. `doi:10.1109/WEMDCD.2013.6525162`.

[11] J. Wang, V.I. Patel, and W. Wang. Fractional-slot permanent magnet brushless machines with low space harmonic contents. *IEEE Trans. Magn.*, 50:1–9, 2014. `doi:10.1109/TMAG.2013.2280883`.

[12] A.M. El-Refaie. Fractional-slot concentrated-windings synchronous permanent magnet machines: Opportunities and challenges. *IEEE Trans. Ind. Electron.*, 57:107–121, 2010. `doi:10.1109/TIE.2009.2030211`.

[13] P. Salminen. *Fractional Slot Permanent Magnet Synchronous Motors for Low Speed Applications*. Lappeenrannan Teknillinen Yliopisto, Lappeenranta, Finland, 2004.

[14] G. De Donato, F. Giulii Capponi, G.A. Rivellini, and F. Caricchi. Integral-slot versus fractional-slot concentrated-winding axial-flux permanent-magnet machines: Comparative design, fea, and experimental tests. *IEEE Trans. Ind. Appl.*, 48:1487–1495, 2012. `doi:10.1109/TIA.2012.2210011`.

[15] G. Zhao, W. Hua, X. Zhu, and G. Zhang. The influence of dummy slots on stator surface-mounted permanent magnet machines. *IEEE Trans. Magn.*, 53:1–5, 2017. `doi:10.1109/TMAG.2017.2658938`.

[16] A. Jabbari. The effect of dummy slots on machine performance in brushless permanent magnet machines: An analytical, numerical, and experimental study. *Iran. J. Electr. Electron. Eng.*, 18:1–11, 2022. `doi:10.22068/IJEEE.18.2.2284`.

[17] I. Hasan, Y. Sozer, A.P. Ortega, S. Paul, and R. Islam. Investigation of design based solutions to reduce vibration in permanent magnet synchronous machines with low order radial forces. In *Proceedings of the 2017 IEEE Energy Conversion Congress and Exposition (ECCE)*, pages 5431–5437, Cincinnati, OH, USA, 2017. IEEE. `doi:10.1109/ECCE.2017.8096908`.

[18] M. Soyaslan, Y. Avsar, A. Fenercioglu, and O. Eldogan. Cogging torque reduction in external rotor pm synchronous motors by optimum pole embrace. In *Proceedings of the 2019 3rd International Symposium on Multidisciplinary Studies and Innovative Technologies (ISMSIT)*, pages 1–4, Ankara, Turkey, 2019. IEEE. `doi:10.1109/ISMSIT.2019.8932915`.

[19] P. Upadhayay and K.R. Rajagopal. Torque ripple reduction using magnet pole shaping in a surface mounted permanent magnet bldc motor. In *Proceedings of the 2013 International Conference on Renewable Energy Research*

and Applications (ICRERA), pages 516–521, Madrid, Spain, 2013. IEEE. `doi:10.1109/ICRERA.2013.6749809`.

[20] T.-W. Kim and J.-H. Chang. Influence of cogging torque reduction method on torque ripple in a surface-mounted permanent magnet synchronous motor. *J. Magn.*, 17:109–114, 2012. `doi:10.4283/JMAG.2012.17.2.109`.

[21] A.N. Patel and A. Kapil. Analysis of cogging torque reduction by increasing stator slot depth in brushless dc motor. In *Proceedings of the 2016 IEEE 1st International Conference on Power Electronics, Intelligent Control and Energy Systems (ICPEICES)*, page 242, Delhi, India, 2016.

[22] S.H. Lee, J.P. Hong, S.M. Hwang, W.T. Lee, J.Y. Lee, and Y.K. Kim. Optimal design for noise reduction in interior permanent-magnet motor. *IEEE Trans. Ind. Appl.*, 45:1954–1960, 2009. `doi:10.1109/TIA.2009.2031905`.

[23] A. Saxena and B.G. Fernandes. Noise and cogging torque reduction in brushless dc ceiling fan. In *Proceedings of the 2015 18th International Conference on Electrical Machines and Systems (ICEMS)*, pages 1334–1338, Pattaya, Thailand, 2015. IEEE. `doi:10.1109/ICEMS.2015.7385246`.

[24] M. Sumega, P. Rafajdus, and M. Stulrajter. Current harmonics controller for reduction of acoustic noise, vibrations and torque ripple caused by cogging torque in pm motors under foc operation. *Energies*, 13:2534, 2020. `doi:10.3390/en13102534`.

[25] Z. Zhong, S. Jiang, Y. Zhou, and S. Zhou. Active torque ripple reduction based on an analytical model of torque. *IET Electr. Power Appl.*, 11:331–341, 2017. `doi:10.1049/iet-epa.2016.0475`.

[26] W. Qian, S.K. Panda, and J.-X. Xu. Torque ripple minimization in pm synchronous motors using iterative learning control. *IEEE Trans. Power Electron.*, 19:272–279, 2004. `doi:10.1109/TPEL.2003.820537`.

[27] A. Gómez-Espinosa, V.M. Hernández-Guzmán, M. Bandala-Sánchez, H. Jiménez-Hernández, E.A. Rivas-Araiza, J. Rodríguez-Reséndiz, and G. Herrera-Ruíz. A new adaptive self-tuning fourier coefficients algorithm for periodic torque ripple minimization in permanent magnet synchronous motors (pmsm). *Sensors*, 13:3831–3847, 2013. `doi:10.3390/s130303831`.

[28] X. Zhang, H. Liu, Z. Zhan, Y. Wu, W. Zhang, M. Taha, and P. Yan. Modelling and active damping of engine torque ripple in a power-split hybrid electric vehicle. *Control. Eng. Pract.*, 104:104634, 2020. `doi:10.1016/j.conengprac.2020.104634`.

[29] S.M. Kuo and D.R. Morgan. Active noise control: A tutorial review. *Proc. IEEE*, 87:943–975, 1999. `doi:10.1109/5.763310`.

[30] M. Shen, F. Xie, W. Zhang, and J. Zhang. Torque ripple reduction of permanent magnet synchronous motor based on least mean square algorithm. In *International Joint Conference on Energy, Electrical and Power Engineering*, pages 638–646, Singapore, 2023. Springer. `doi:10.1007/978-981-99-4334-0_79`.

[31] Marco Bassani, Daniel Pinardi, Andrea Toscani, Elisabetta Manconi, and Carlo Concari. Active vibration control via current injection in electric motors. *Electronics*, 13(17), 2024. URL: `https://www.mdpi.com/2079-9292/13/17/3442`, `doi:10.3390/electronics13173442`.

[32] N. Rocchi, A. Toscani, G. Chiorboli, D. Pinardi, M. Binelli, and A. Farina. Transducer arrays over a2b networks in industrial and automotive applications: Clock propagation measurements. *IEEE Access*, 9:118232–118241, 2021. `doi:10.1109/ACCESS.2021.3106710`.

[33] C. Belicchi, A. Opinto, M. Martalo, A. Tira, D. Pinardi, A. Farina, and G. Ferrari. Anc: A low-cost implementation perspective. In *SAE Technical Papers*, Warrendale, PA, USA, 2022. SAE International. `doi:10.4271/2022-01-0967`.

[34] E. Voltolini, D. Pinardi, A. Toscani, M. Binelli, A. Farina, J. Ferrari, S. Maglia, A. Zenaro, and E. Calzavacca. Design of an active noise reduction system for a cogeneration plant. In *Proceedings of the 2023 Immersive and 3D Audio: From Architecture to Automotive (I3DA)*, pages 1–7, Bologna, Italy, 2023. IEEE. `doi:10.1109/I3DA57090.2023.10289192`.

[35] Rosalba Simeone and Antonio Montepara. Reducing co2 emissions in transportation systems: technologies for electric vehicles powering. *Transportation Research Procedia*, 74:1094–1101, 2023.

[36] Rosalba AL Simeone and Antonio AL Monetepara. The dynamic wireless power transfer project: the experimental development of an innovative technology towards the decarbonisation of transportation systems. 2023.

[37] Rosalba Simeone and Antonio Montepara. Recharge traveling: The electric road system. In *International Conference on Transportation and Development 2023*, pages 310–319, 2023.

Acknowledgement

Essendo per forza di cose l'ultima tesi che conclude un percorso abbastanza lungo piu che una semplice lista di ringraziamenti penso sia corretto ricordare gli eventi e le persone che per un modo o per l'altro hanno fatto si di trovarmi qui a concludere il dottorato in ingegneria elettronica o che mi hanno accompagnato in questo lungo periodo di studi. Innanzitutto potrebbe essere scontato ma non lo è fino quando non lo si dice ma senza la pazienza e l'appoggio di mio papà e mia mamma assolutamente non sarei qui, questo perchè in questi 30 anni, nelle mie scelte sono stato guidato sempre da molta curiosità verso realtà "abbastanza particolari" e fuori norma che mi hanno portato a dedicare diverse stanze della casa a laboratori e nonostante questo disagio hanno sempre assecondato le mie scelte tante volte folli.

Crescendo in realtà contadine, grazie a mia nonna Adele, Dina e soprattutto grazie a mio nonno Nino sono sempre stato abituato a parlare il dialetto e girare in officina per aggiustare di tutto pur di non buttare via macchine guaste, e sono cresciuto con la fatidica frase nelle orecchie "tienilo che può servire"; risultato che poi non serve mai. Da qui probabilmente la vicinanza sempre più a percorsi scientifici rispetto a quelli umanistici.

Le prime macchine che hanno segnato l'inizio di un grosso fascino verso l'elettromeccanica già alle elementari sono stati i vecchi contatori elettrici ad induzione in quanto in quel periodo a cavallo del 2002 l'Italia con l'ENEL lanciò per prima in tutto il mondo la campagna di sostituzione dei misuratori tradizionali con gli smart meters. Era chiaro quanto l'elettronica e l'informatica fossero mature e quanto ormai stessero modificando radicalmente l'approccio ai problemi, passando da strumenti complicati e costosi dove l'ingegno stava nel riuscire a sfruttare e plasmare i vari principi della fisica noti in letteratura per risolvere i problemi più disparati, verso un modo di affrontare le cose totalmente diverso, cercando di abbandonare il più possibile l'utilizzo della fisica andando a spostare l'ingegno negli algoritmi di elaborazione dei dati prima in modo elettronico e poi via firmware.

Contemporaneamente la curiosità verso le centrali telefoniche automatiche decadiche gli strumenti ad indice mobile quali tachimetri magnetici, strumenti a bobina mobile, ferro mobile ed elettrodinamici hanno dato il colpo finale rendendo chiara la futura scelta per l'ITIS elettrotecnico dove ho lasciato il cuore e a cui devo tanto per la preparazione tecnica che ho ora, in particolare devo ringraziare il mio prof. di elettrotecnica Giuseppe per aver sempre cercato di rispondere alle mie domande facendomi amare quello che studiavo.

Devo ammettere che ho trovato tante persone che senza essere tenute a farlo, hanno fatto, secondo loro poco, ma per me tanto insegnandomi e togliendomi delle curiosità che in quel particolare momento erano delle grandi curiosità... ad esempio Luca che alle medie mi ha fatto un corso sulla rete di distribuzione e i sistemi di misurazione del metano o la signora Cavalca, Pasquale e soprattutto Matteo che a 15 anni mi hanno insegnato il mestiere del proiezionista cinematografico potendo vivere la magia del cinema che ancora oggi è la mia più grande passione nonostante tutto sia stato ormai svuotato di significato con la proiezione digitale.

Un altro periodo molto costruttivo è stato quello a cavallo dei 20 anni dove avevo un obiettivo molto grande in cui credevo, quello di conoscere tutti i segreti della fotografia analogica, sviluppo e stampa e perciò devo ringraziare la Stefi che per anni mi ha portato in laboratorio insegnandomi veramente tanto della fotografia tradizionale, e anche se ora con il digitale tante nozioni sulla matematica e la fisica dietro la fotografia sembrino non più necessarie in realtà tutto ciò mi ha lasciato tanto anche professionalmente.

Per assurdo una delle motivazioni che hanno fatto si di farmi iscrivere ad ingegneria elettronica è stata la curiosità ormai più che ventennale per la registrazione audio/video magnetica, che mi ha spinto verso questa scelta perchè avevo un obiettivo, quello di riparare a tutti i costi i videoregistratori usati per la messa in onda televisiva e i registratori a bobine usati per il mastering in sala incisione, mi trovai quindi costretto a doverlo fare personalmente non essendoci ormai più laboratori specializzati in riparazione di queste macchine. Devo ringraziare quindi queste macchine se ho basato tre tesi sul controllo dei motori elettrici perchè il controllo automatico del posizionamento delle testine video sulle tracce magnetiche registrate sul nastro è sempre stato un concetto fortemente affascinante e assurdo che mi mancava da capire.

Decisamente un grande ringraziamento va alla categoria dei ferrovieri, dai giovani ai meno giovani, macchinisti, capitreno, dirigenti movimento e tecnici di infrastruttura che nei tanti anni mi hanno accompagnato (un po' sopportato) e mi hanno risposto a tante curiosità soprattutto riguardo uno spaccato di ferrovia del passato che è ormai al termine e non tornerà più, permettendomi finalmente di chiudere una passione durata 15 anni. Questa passione senza volere mi ha lasciato tanto, è iniziata con curiosità riguardo "pezzi di ferro" ma mi ha fatto incontrare e conoscere tante persone meravigliose. Un ringraziamento speciale ai miei "maestri" Nello, Demetrio, Alberto, Antonio, Andrea, Pino, Max, Massimo, Jacopo, Diego, Giulio... la lista è lunga.

Il dottorato, nonostante i primi due anni nel pieno del progetto siano stati abbastanza impegnativi, ha fatto si grazie alle varie lezioni e conferenze di essere circondato da ragazzi e ragazze che hanno reso questa esperienza comunque un bel ricordo, come il gruppo "Giacoma" con Isa, Lara, Mandrio, Laura, Bucci, o i compagni di sventura del "B2" Tiziana, Biagio, Fausto, Anila, e poi anche Rosalba, Ambra, Antonio e tutto il gruppo informatico. Sono stato veramente felice di aver potuto insegnare elettrotecnica per tre anni e anzi è forse stata l'esperienza che più mi ha dato soddisfazione durante tutto questo periodo, perchè è emozionante rendersi conto che per quei ragazzi che si approcciano per la prima volta ad una materia, l'attenzione dell'aula in quel momento dipende solo da te, non da quello che scrivi alla lavagna ma da quello che dici, e mi rendo conto di aver "tirato fuori dal cappello" di bei racconti trovandomi a spiegare tensioni, correnti, resistori e induttori con palazzi alti o bassi, tubi dell'acqua, porte piccole o grosse e auto ferme da spingere. Tutto ciò ha portato col tempo a coltivare dei bei rapporti con studenti come ad esempio il Ferra.

Un particolare ringraziamento va a tutto il gruppo della palazzina 4, a chi è andato e a chi è rimasto, e al gruppo "La giuria" che hanno accompagnato questa esperienza giorno dopo giorno. Voglio ringraziare i prof. Nicola Delmonte e Paolo Cova ma soprattutto una delle menti più brillanti che abbia conosciuto, Danilo Santoro, per avermi coinvolto in alcuni progetti che sono diventati poi l'attuale lavoro del mio Post-doc.

Anche se passato tanto tempo mi fa piacere ricordare tutti quei ragazzi con cui ero in corso ai tempi delle lezioni e con cui ho condiviso tanti caffè e paranoie degli esami e che purtroppo, il tempo ci ha divisi. Allo stesso modo, ho condiviso veramente tante giornate con tutti i ragazzi e ragazze che negli anni sono passati prima in biblioteca a Casalmaggiore e poi in OIC, anche in questo caso con il tempo si dimenticano tante cose ma senza queste persone sarebbe stato tutto più triste e monotono, in particolare voglio ringraziare Scara, Ale e Botto per aver dato una piega molto positiva a quei momenti indimenticabili e non potrei non ricordare, i bibliotecari Santina, Vittorio ma soprattutto la Sandra che mi ha sempre permesso di fare tutto in quella biblioteca, dal caos al bibliotecario.

Dovendomi spostare fin dalle superiori è inevitabile aver passato una quantità di tempo non trascurabile viaggiando, e negli anni veramente tante amicizie sono iniziate durante i viaggi e i disagi in treno e proseguite giù. Sono stato quindi contento di aver conosciuto L'elena, Loris, la Vale, Anastasia e Maricla. Allo stesso tempo è stato anche inevitabile vedere il lato debole della nostra società che si cerca sempre di cancellare ma c'è eccome e anche abbastanza grande a tal punto di abituarsi rendendo così invisibili tutte queste persone, ma ho potuto anche vedere una bellissima cosa, le postazioni dei "City Angels" che da anni presiedono la stazione di Parma nelle ore serali per distribuire pasti e altro a chi ne ha bisogno. Questo è stato più volte motivo di riflessione perchè spesso o quasi sempre si da per scontato il ruolo fondamentale che i volontari di qualsiasi categoria abbiano in un paese.

In ultimo non per importanza ma perchè esulano dalla cronologia dei fatti, ho piacere ricordare i vari gruppi di ragazzi che nonostante con alcuni le strade si siano separate, in un certo periodo hanno avuto un ruolo importante e hanno lasciato emozioni indelebili, come il gruppo "del Tango", "dei 94 del Lido", "dei meccanici", "dei Viadanesi", "dei Gussolesi", "dei finferli" e la Rosa, ma soprattutto amicizie ormai di vecchia data su cui ho sempre potuto contare come Roby, Andre, Lara, Tego, Rambo, Sonny, Cozza, Lazzaro, Greg. Il Raccio e il Pelux per tutte quelle birre bevute su quel balcone e il Tranci e il Ciro per tutte quelle notti in bianco parlando di tutto o guardando chilometri di pellicola scorrere.

Dal punto di vista accademico devo ringraziare il supporto dell'azienda Casappa S.p.A per la quale mi sono occupato dell'elettrificazione del loro fan-drive e in particolare gli ingegneri Loris, Alessandro, Paolo e Nicola, che nonostante i tantissimi imprevisti durante lo sviluppo del prodotto e la notevole tensione per le scadenze hanno sempre cercato di venirmi incontro e di trovare soluzioni. Il tutor Carlo Concari e Andrea Toscani per avermi accompagnato nelle tre tesi, Alessandro Soldati per avermi dato un enorme aiuto sia in termini di concetti sia di metodo scientifico per l'approccio ai problemi, nonostante la pensassimo spesso in modo diverso, e a Matteo Dalboni che è sempre stato estremamente disponibile quando avessi un problema di controlli automatici. Dopo tutti gli anni passati nei laboratori un grande ringraziamento al tecnico Luca da cui ho imparato tanto e senza di lui tanti progetti non sarebbero riusciti così bene, purtroppo ora in pensione è una grande perdita per la didattica. Questi 10 anni in Università mi hanno dato anche la possibilità di conoscere professori, soprattutto di una certa epoca, che da studente non ero stato in grado di apprezzare per modi e metodi magari anche un po' discutibili ma col senno di poi mi rendo conto di aver potuto conoscere dei professionisti.

Riflettendo sulle varie curiosità che ho avuto, anche un po' anacronistiche ma da cui ho imparato tanto, mi è sempre più chiaro quanto per noi oggi con l'aiuto dei mezzi potentissimi che abbiamo e che spesso diamo per scontati sia decisamente più semplice plasmare la fisica a nostro piacimento e ottenere gli stessi risultati che magari anni fa erano grossi problemi che solo le aziende leader del settore erano in grado di risolvere, ma soprattutto quanto sia sempre più possibile "andare oltre", spingendoci a livelli ormai impressionanti. Appunto considerando questo ho imparato ad apprezzare le macchine e gli strumenti con i loro limiti, non tanto per i risultati che riescono ad ottenere ma sul come li ottegono e sulla fatica che i progettisti hanno impiegato per raggiungere magari quello che per noi oggi è scontato.